

## Turbulent Mixing During Late Summer in the Ice–Ocean Boundary Layer in the Central Arctic Ocean: Results From the MOSAiC Expedition

Yusuke Kawaguchi<sup>1</sup> , Zoé Koenig<sup>2,3</sup> , Daiki Nomura<sup>4,5,6</sup> , Mario Hoppmann<sup>7</sup> , Jun Inoue<sup>8</sup> , Ying-Chih Fang<sup>7,9</sup> , Kirstin Schulz<sup>7,10</sup> , Michael Gallagher<sup>11,12</sup> , Christian Katlein<sup>7</sup> , Marcel Nicolaus<sup>7</sup> , and Benjamin Rabe<sup>7</sup> 

<sup>1</sup>Atmosphere and Ocean Research Institute, The University of Tokyo, Chiba, Japan, <sup>2</sup>Norwegian Polar Institute, Tromsø, Norway, <sup>3</sup>Bjerknes Center for Climate Research, Geophysical Institute, The University of Bergen, Bergen, Norway, <sup>4</sup>Field Science Center for Northern Biosphere, Hokkaido University, Hakodate, Japan, <sup>5</sup>Faculty of Fisheries Sciences, Hokkaido University, Hakodate, Japan, <sup>6</sup>Arctic Research Center, Hokkaido University, Sapporo, Japan, <sup>7</sup>Alfred-Wegener-Institut Helmholtz-Zentrum für Polar- und Meeresforschung, Bremerhaven, Germany, <sup>8</sup>National Institute of Polar Research, Tokyo, Japan, <sup>9</sup>National Sun Yat-sen University, Kaohsiung, Taiwan, <sup>10</sup>Oden Institute for Computational Engineering and Sciences, The University of Texas at Austin, Austin, TX, USA, <sup>11</sup>Physical Sciences Laboratory, National Oceanic and Atmospheric Administration, Boulder, CO, USA, <sup>12</sup>Cooperative Institute for Research in Environmental Science, Boulder, CO, USA

### Key Points:

- Enhanced ice drift and near-surface freshened water jointly promoted early termination of basal melting and preconditioning of refreezing
- Turbulent dissipation rate can be scaled by 1.4–1.7 times of the “*Law of the Wall*” criterion, with surface buoyancy flux being negligible
- Near-inertial wave was trapped by weakly stratified water in lower mixed layer, which produced turbulence by the Holmboe instability

### Correspondence to:

Y. Kawaguchi,  
[ykawaguchi@aori.u-tokyo.ac.jp](mailto:ykawaguchi@aori.u-tokyo.ac.jp)

### Citation:

Kawaguchi, Y., Koenig, Z., Nomura, D., Hoppmann, M., Inoue, J., Fang, Y.-C., et al. (2022). Turbulent mixing during late summer in the ice–ocean boundary layer in the central Arctic Ocean: Results from the MOSAiC expedition. *Journal of Geophysical Research: Oceans*, 127, e2021JC017975. <https://doi.org/10.1029/2021JC017975>

Received 2 SEP 2021  
Accepted 14 JUL 2022

**Abstract** We examined mixing processes within the ice–ocean boundary layer (IOBL) close to the geographic North Pole, with an emphasis on wind-driven sea ice drift. Observations were conducted from late August to late September 2020, during the final leg of the international Multidisciplinary drifting Observatory for the Study of Arctic Climate (MOSAiC) expedition. Measurements of ice motion, and profiles of currents, hydrography, and microstructure turbulence were conducted. The multifarious direct observations of sea ice and the upper ocean were used to quantify the transport of momentum, heat, and salt in the IOBL. The ice drift was mostly characterized by the inertial oscillation at a semi-diurnal frequency, which forced an inertial current in the mixed layer. Observation-derived heat and salinity fluxes at the ice–ocean interface suggest early termination of basal melting and transitioning to refreezing, resulting from a rise in the freezing point temperature by the presence of freshened near-surface water. Based on the friction velocity, the measured dissipation rate ( $\epsilon$ ) of turbulent energy can be approximated as 1.4–1.7 times of the “*Law of the Wall*” criterion. We also observed a spiraling Ekman flow and find its vertical extent in line with the estimate from  $\epsilon$ -based diffusivity. Following passage of a storm, the enhanced oscillatory motions of the ice drift caused trapping of the near-inertial waves (NIWs) that exclusively propagated through the base of the weakly stratified mixed layer. We accounted Holmboe instabilities and NIWs for the observed distinct peak of the dissipation rate near the bottom of the mixed layer.

**Plain Language Summary** We examined how sea ice drift in the Arctic Ocean affects the movement of seawater directly under the ice, and how this impacts freezing and melting of the ice itself. During the Multidisciplinary drifting Observatory for the Study of Arctic Climate expedition, we used a number of different instruments to measure air, sea ice and ocean properties on an ice floe between late August and late September 2020. We recorded the drift tracks of the ice, and linked the ice motion to the currents, temperature and salinity within the upper 50 m of the ocean. Strong winds triggered wavy fluctuations and water mixing, in particular close to where the ice and ocean meet. During a storm in mid-September, the ice stopped melting and started to refreeze even though the water and the air were still relatively warm. We explain this by the presence of surface water that was less salty, and therefore froze faster at higher temperature, and by the ice moving faster than usually observed in the region. In combination, these factors provided favorable conditions for sea ice formation. Our results suggest that the distribution of sea ice meltwater need to be accounted for in order to better predict Arctic sea ice conditions in the future.

## 1. Introduction

In recent decades, sea ice drift has been increasing in the Arctic Ocean as a response to enhanced surface winds (Rampal et al., 2009, 2011). This is partially due to the weakened internal stress between ice floes for the low sea ice concentration, characterized by reduced lateral friction and less-frequent collision (Leppäranta, 2005).

© 2022. The Authors.

This is an open access article under the terms of the [Creative Commons Attribution-NonCommercial-NoDerivs License](https://creativecommons.org/licenses/by-nc-nd/4.0/), which permits use and distribution in any medium, provided the original work is properly cited, the use is non-commercial and no modifications or adaptations are made.

In general, the thermal and kinematic energy of the ice–ocean boundary layer (IOBL) is strongly dependent on sea ice drift through the turbulent fluxes across the IOBL (e.g., Hunkins, 1966; McPhee, 2008a, 2008b; Sirevaag, 2009; Kawaguchi et al., 2012). In particular, the inertial motion of ice drift can amplify the inertial oscillation in the surface mixed layer (SML) (D’Asaro, 1985; Martini et al., 2014) and further excite the generation of internal waves at similar frequencies that travel to greater depths (e.g., Halle & Pinkel, 2003; Kawaguchi et al., 2016; Martini et al., 2014; Pinkel, 2005).

The coupling of drifting ice and the near-surface ocean can influence the thermodynamic growth and decay of the sea ice through turbulent heat and salt fluxes at the ice–ocean interface (e.g., McPhee, 2008a; McPhee & Martinson, 1994; Shaw et al., 2009; Sirevaag, 2009). The development of IOBL turbulence can also be affected by the buoyancy flux at the interface caused by fresh water intrusion from melting sea ice, and brine rejection during sea ice development. For the stable surface condition during summer, the relation between ice melting and turbulent heat flux through ice drift has garnered much attention from researchers in the context of global warming (e.g., Fer, 2006; Kawaguchi et al., 2012, 2016; Vivier et al., 2016). Investigations on the unstable situation of brine rejection during ice formation in leads were conducted in some earlier studies (e.g., McPhee & Stanton, 1996). During the transitional phase of a stable-to-unstable ice–ocean interface, the joint effects of mechanical and buoyancy-driven entrainment are, however, not well understood yet, while most studies were made in ice-free water (e.g., Lombardo & Gregg, 1989; Lozovatsky et al., 2005; Oakey & Elliot, 1982).

From October 2019 to October 2020, the international ship-based observational campaign “Multidisciplinary drifting Observatory for the Study of the Arctic Climate” (MOSAiC) expedition was conducted by the German icebreaker RV Polarstern in the central Arctic Ocean (Figure 1a) (e.g., Nicolaus et al., 2022; Rabe et al., 2022; Shupe et al., 2022, 2020). During the last leg (Leg 5) in August–October 2020, Polarstern returned to the central Arctic Ocean from Fram Strait after the conclusion of their first drift, installing a new ice camp close to the geographical North Pole. In this study, we use data from this final leg of MOSAiC to examine dynamical and thermodynamical aspects of the IOBL as it transitioned from melting to refreezing. We obtain a comprehensive and quantitative understanding of the processes in the IOBL by combining various observational datasets of sea ice drift, physical oceanography (hydrography, current, and turbulence), and sea ice mass balance.

Our main objective of this study is to quantify the thermodynamic growth and decay of the consolidated pack ice from the viewpoint of heat and salt exchange by turbulence. In relation to the inertial ice drift, the generation and propagation of near-inertial waves (NIWs) are explored based on the observations. In particular, we focus on the dissipation rate of turbulent kinetic energy (TKE),  $\epsilon$ , in the context of energy sources: stress-induced shear, buoyancy-driven convection, and shear instability from internal wave activity.

This paper is structured as follows: Section 2 summarizes the observational program and data processing techniques. In Section 3, the prevailing atmosphere, sea ice and ocean conditions at the study site are briefly reviewed. In the same section, turbulent boundary fluxes with respect to temperature, salinity and buoyancy are estimated from the local turbulence closure (LTC) equations. In Section 4, the generation of inertial oscillations in the SML is addressed with a SML slab model, along with a detailed analysis of NIW activity. In Section 5, we investigate variables in association with turbulence derived from the microstructure measurements, with a focus on a storm event in mid-September. In particular, the observed profiles of  $\epsilon$  are scaled by the *Law of the Wall* (*LoW*) model, and also compared with the shear production term in the TKE balance. Section 6 summarizes the overall findings from this study.

## 2. Observational Program and Data Processing

The observations were conducted during Leg 5 of the MOSAiC expedition, between 23 August and 18 September 2020. The study site was an individual ice floe in a consolidated pack ice field, initially located at 87.74°N, 105.41°E.

Horizontal distribution of sea ice draft, including the depth of sea ice keels, was obtained from a multi-beam sonar installed on a remotely operated vehicle (ROV; Katlein et al., 2020; 2022) (Figure 1b). During MOSAiC Leg 5, the ROV was operated within a distance of ~200 m through a hydrohole, located at  $x = 50$  m and  $y = -110$  m, toward the ship. The observed bottom topography during a dive on 5 September 2020 showed

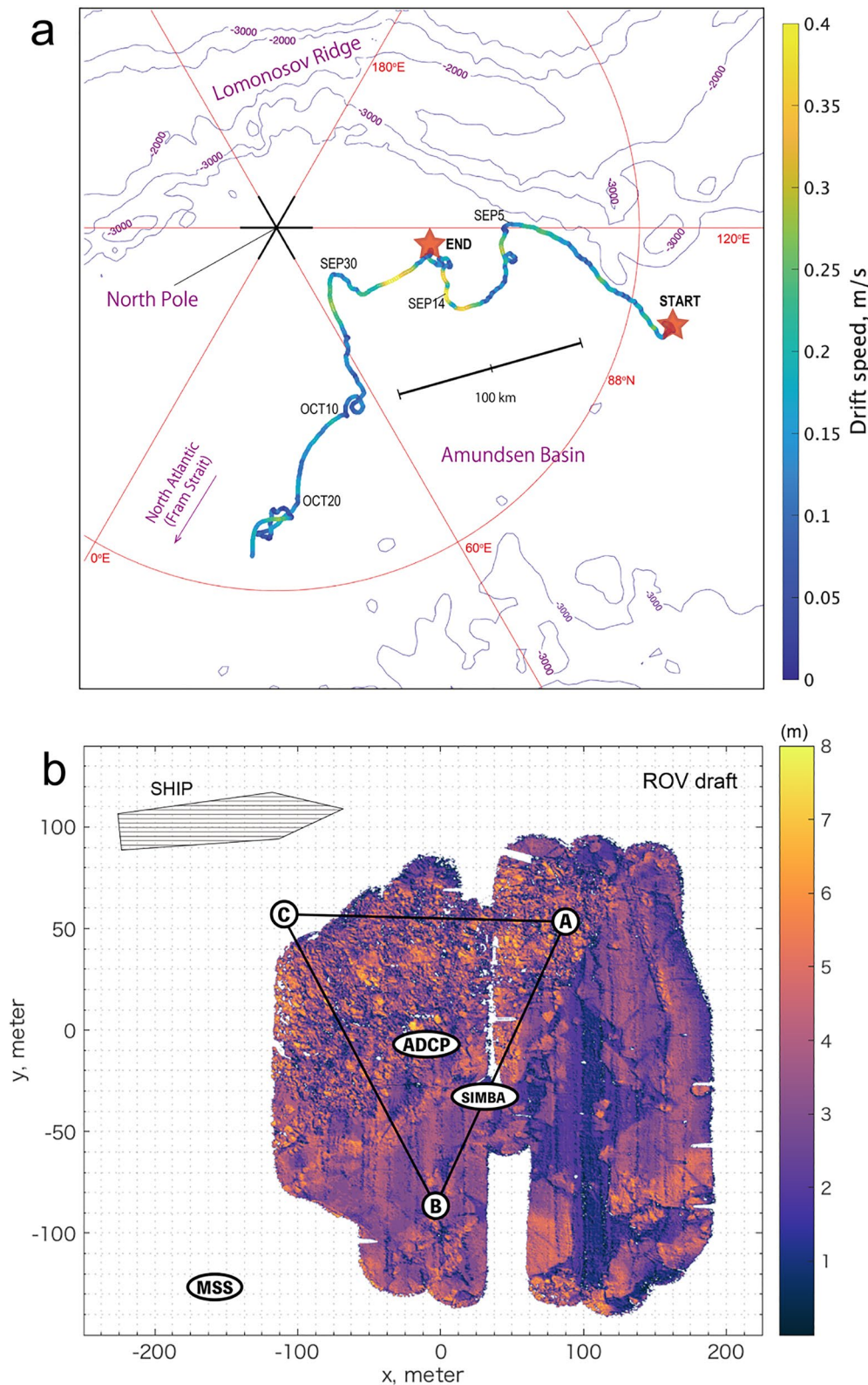


**Figure 1.** (a) Drift trajectory of the ice flow, where locations of start on 23 August and end on 18 September of the MOSAiC Leg5 are marked by red stars. The colors indicate the drift speed, the labels along the track indicate the date in 2020. Bathymetry contours are taken from the ETOPO1 (NOAA National Geographic Data Center). (b) Locations of relevant sites in the ice camp, along with ROV-based sea ice draft. A, B, and C = ice tracking buoys; ADCP = current profiler; SIMBA = ice mass balance buoy; MSS = microstructure site (Ocean City).

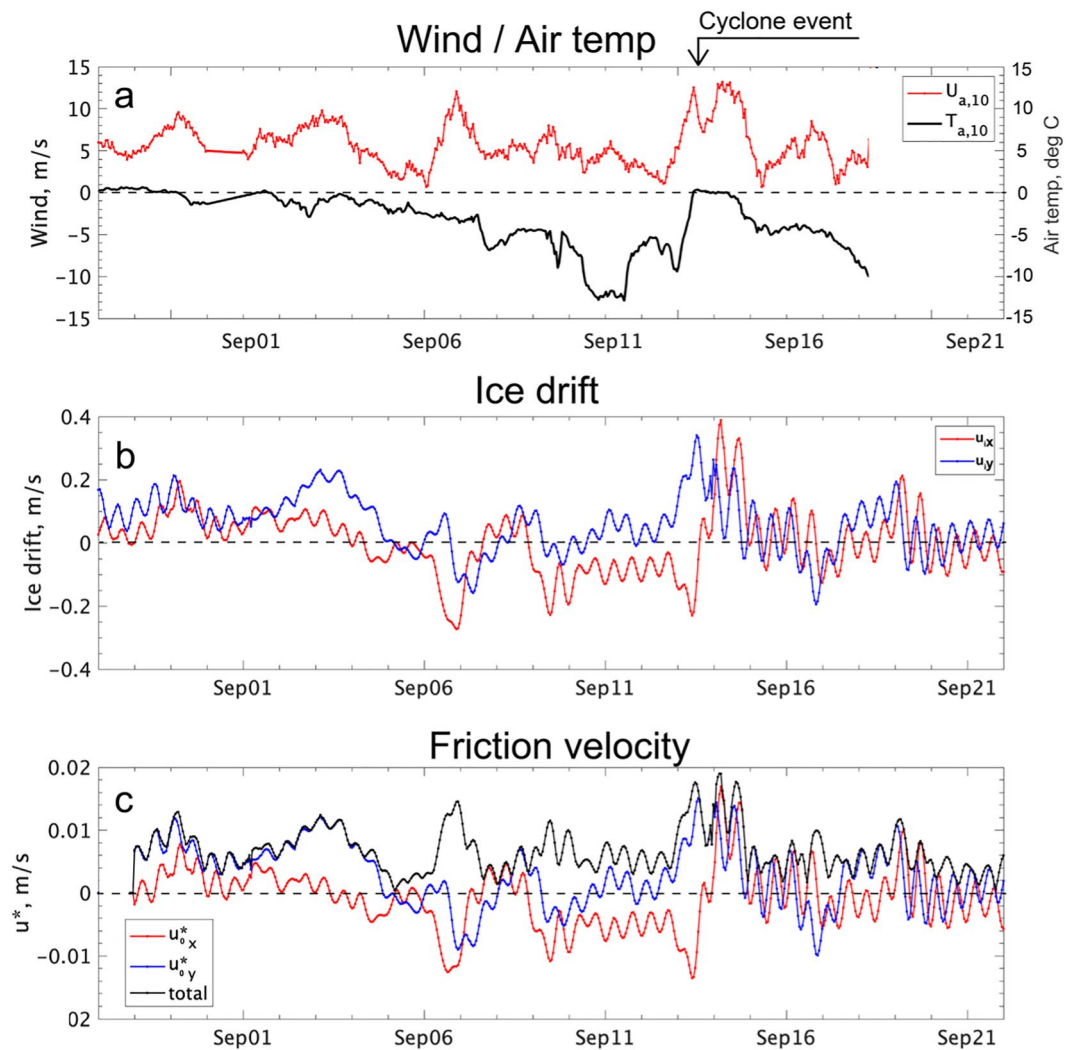


**Figure 2.** Time series of (a) 10-m wind magnitude (red) and air temperature (black), (b) ice drift  $U_i = (U_{ix}, U_{iy})$  and (c) interfacial friction velocity  $u_0^* = (u_{0x}^*, u_{0y}^*)$ , where zonal and meridional components are represented in red and blue, respectively. In (c), the root-mean-square values of the horizontal components are shown in black.

that the ice field was highly deformed in the vicinity of the Acoustic Doppler Current Profiler (ADCP) (Figure 1b). The mean ice thickness was 2.9 m, with an interquartile range (IQR), defined hereinafter as a difference between the first and third quartiles, of 0.17 m near where Polarstern was moored. The area around the MSS tent was out of the ROV's surveillance, so the ice draft distribution at this site cannot be fully assessed. Manual observations showed that the ice there was relatively level and  $\sim 1.5$  m thick on average.

### 2.1. Sea Ice Drift

Ice drift was measured using a buoy array of GPS ice trackers (IceST/20DP; Marlin-Yug, Russia) (Kawaguchi et al., 2021b). The array contained three buoys which were installed on the ice between the peak of the triangle shown in Figure 1b, with an integrated system of current meters installed approximately in the center of the array. The GPS location at each buoy was transmitted every 10 min, and the uncertainty of the horizontal position is about 10 m. The horizontal velocity of sea ice is estimated from the temporal differentials for each ice tracker (Figure 2b). Sea ice tracking measurements began on 2 September 2020 and continued until the end of the year, even after the ship left the site on September 21.

The ice–ocean friction velocity vector,  $\mathbf{u}_0^*$ , is estimated from the ice drift (Figure 2c). It is computed based on the Rossby's similarity equation for the neutral stratification (McPhee, 2008a), given by

$$\frac{\mathbf{U}_i}{\mathbf{u}_0^*} = \frac{1}{\kappa} \left( \log \frac{\mathbf{u}_0^*}{f z_0} - A \mp iB \right) \quad (1)$$

where  $f$  is the Coriolis frequency,  $\kappa$  is von Kármán's constant (0.4), the constants  $A$  and  $B$  are 2.3 and 2.1, respectively (McPhee, 2008a),  $z_0$  is the hydraulic roughness, and  $\mathbf{U}_i$  is the ice drift velocity vector. The definition of  $\mathbf{u}_0^*$  and  $\mathbf{U}_i$  are complex quantities, adapted as  $\mathbf{u}_0^* = u_{0x}^* + iu_{0y}^*$  and  $\mathbf{U}_i = U_{ix} + iU_{iy}$  with their corresponding components along the  $x$  and  $y$  directions. ( $i = \sqrt{-1}$ ). Note that we use the plain font to indicate the magnitude of a vector quantify (e.g.,  $u_0^* = |\mathbf{u}_0^*|$ ) following earlier studies (e.g., Fer & Sundfjord, 2007). The implicit equation above is solved numerically using the MATLAB® optimization toolbox function *fsolve*.

For the roughness, we used a constant value of  $z_0 = 0.01$  m following some related studies (e.g., MCPhee, 2002; Timmermans et al., 2011). MCPhee (2002) suggested the feasible range of  $z_0 = 0.007$ – $0.01$  m derived from near-surface Reynolds stress and current velocity with an ice-based turbulence instrument that resolves the inertial subrange of velocity spectrum. According to our computation based on Equation 1, the mean values of  $u_0^*$  for the entire study period are 0.0064 and 0.0067 m s<sup>-1</sup> for  $z_0 = 0.007$  and 0.01 m, respectively. These two choices of  $z_0$  in Equation 1 could make a difference as large as roughly 16% providing a cubic function of  $u_0^*$  for evaluation of the cross-interface energy flux  $E_0$  (refer to Section 5). Timmermans et al. (2011) used  $z_0 = 0.01$  m for the estimate of  $u_0^*$  with their data of an autonomous observation of a 1.7 m thick multi-year ice near the geographic North Pole during the melting season (similar to our condition). They validated the result from the parameterization by comparison with the velocity eddy-covariance observation. Therefore, the choice of  $z_0 = 0.01$  m in our study is supported by those earlier studies.

## 2.2. Observation and Correction of Water Current

Ocean currents were measured between 23 August and 20 September 2020 using an ADCP (400 kHz AquaDopp; Nortek, Norway) (Kawaguchi et al., 2021a). The downward-looking ADCP was installed through a hole in the ice located at the center of the buoy triangle (labeled “ADCP” in Figure 1b). Its transducer was at a depth of 1.0 m underneath the ice bottom, where the ice draft was measured to be 2.9 m at the time of deployment (Figure 1b). Vertical and temporal resolutions were 2 m and 10 min, respectively. According to the technical specifications, the accuracy of the current velocity is 1% of the measured value, typically  $\pm 0.5$  cm/s. Vertical and horizontal components of the ocean current were obtained at 20 levels, distributed within a depth range of 4–42 m from the level of water surface ( $\sim 1$  m relative to the ice base).

The ADCP's position relative to the ice floe remained unchanged during the study period, although a directional error of  $\sim 5^\circ$ – $8^\circ$  was introduced during the battery changes on 5 and 13 September. This effect was mitigated using the records from the on-board compass. The vertical component of the water movement was calibrated based on the records of pitch and roll derived from the ADCP's built-in tilt sensors. In post-processing of all current data, measurement errors and outliers were detected and discarded for each component, using a cut-off threshold of two standard deviations. Linear interpolation was applied for any missing data. Finally, a 1-hr lowpass filter was applied.

For the water velocity analyses, the original  $X$ – $Y$  Cartesian coordinates were translated to Earth coordinates along the zonal (eastward increasing) and meridional (northward increasing) axes. The original data referencing to the frame of the drifting ice were corrected using the following formula:

$$\mathbf{U}_w = \begin{pmatrix} \cos\theta_0 & -\sin\theta_0 \\ \sin\theta_0 & \cos\theta_0 \end{pmatrix} \mathbf{U}_{w,xy} + \mathbf{U}_i \quad (2)$$

where  $\mathbf{U}_w$  represents the water velocity relative to the ground and  $\mathbf{U}_{w,xy}$  stands for water velocity relative to the ice. The inclination angle  $\theta_0(t)$  of the  $X$  axis is set with an offset of  $33^\circ$ . Its temporal variation is inferred from the rotational rate of the buoy array. Then, a portion of vertically averaged horizontal current over the 30–40 m depth range (representing the geostrophically balanced portion in the raw velocity) was subtracted.

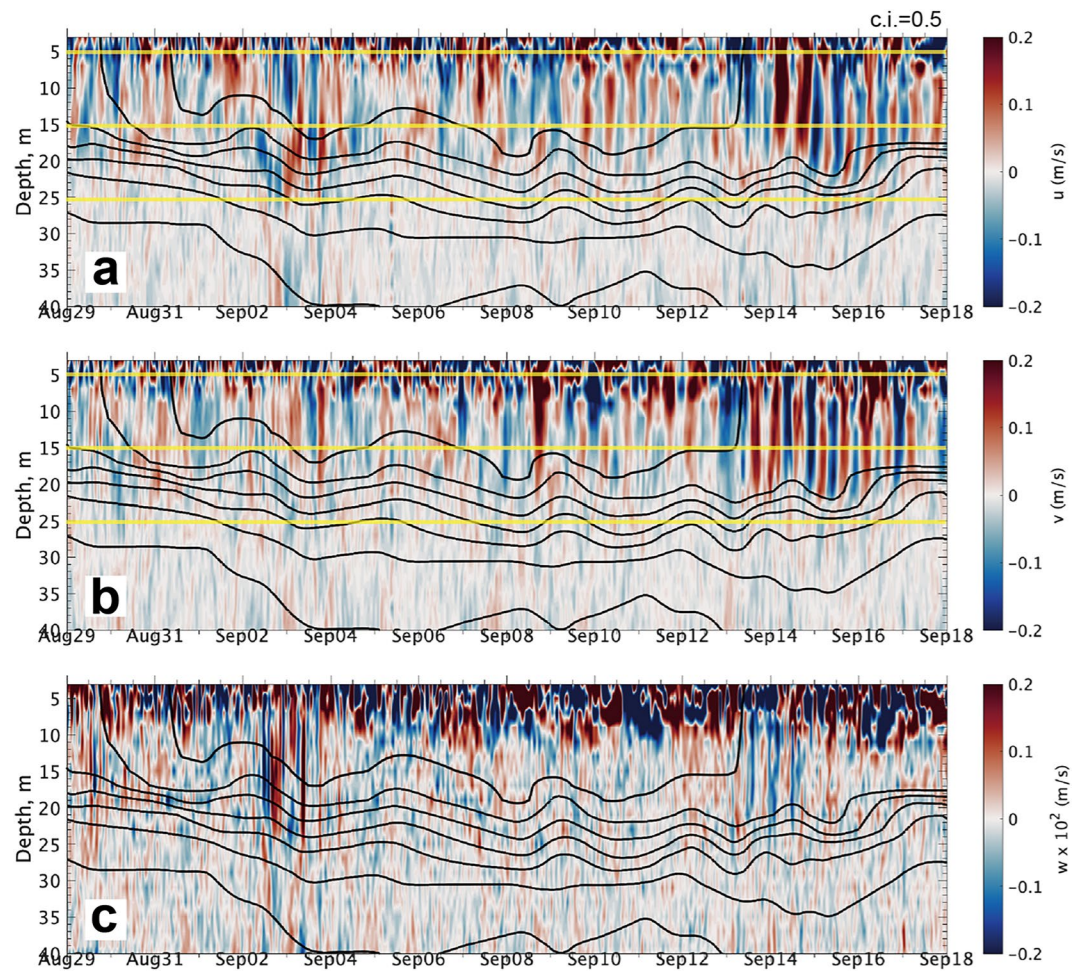


**Figure 3.** The ice–ocean boundary layer-adjusted Acoustic Doppler Current Profiler currents: (a) zonal, (b) meridional, and (c) vertical components, where the vertical velocity is multiplied by 100. Solid contours show  $\sigma_\theta$  at a constant interval of  $0.5 \text{ kg m}^{-3}$ . Yellow, horizontal lines show the depths of 5, 15, and 25 m, for which the spectral calculation is conducted (Figure 12).

In what follows, we will refer to the ADCP horizontal velocity (Figure 3) represented in the coordinate above as “IOBL-adjusted” velocity, and use it throughout the present study.

### 2.3. Hydrography and Turbulence Variables

Hydrographic and turbulence microstructure data were collected using a free-falling tethered profiler (MSS-90L; Sea and Sun Technology, Germany) (Schulz et al., 2022) lowered through a hole located at a distance of  $\sim 150 \text{ m}$  from the ADCP (labeled “MSS” in Figure 1b). The MSS descended to a maximum depth of between 250 and 400 m, depending on cable length and currents, at a sinking speed of about  $0.6 \text{ m s}^{-1}$ . Sensors at the instruments head measures seawater conductivity (SST small), temperature (PT100) and depth (PA7-100) (CTD) with accuracies of  $\pm 0.002 \text{ mS/cm}$ ,  $\pm 0.002^\circ\text{C}$ , and  $\pm 0.1 \text{ dbar}$ , respectively. The response time of the sensors above is approximately 150 ms, resulting in vertical resolution of 5–10 cm for the raw CTD variables. A total of 250 MSS profiles were collected between 22 August and 20 September.

Typically, at least four consecutive profiles were obtained every day, with two periods of continuous profiling during storm events starting on 6 September (33 hr, 97 consecutive profiles) and on 14 September (27 hr, 82 profiles). The later period of intensified sampling, complemented with the regular daily MSS measurements on 13 September, is analyzed in depth in this study (see Table 1).

**Table 1**

Periods and Boundary Conditions for Terms I, II, III, and IV: Mean and Standard Deviation in Parenthesis

|   | Term I                                | Term II                              | Term III                             | Term IV                             |
|---|---------------------------------------|--------------------------------------|--------------------------------------|-------------------------------------|
| Period (start/end) in UTC   | 13 September 10:42/13 September 11:46 | 14 September 4:47/14 September 12:12 | 14 September 13:25/15 September 2:42 | 15 September 3:01/15 September 7:36 |
| # of MSS profiles   | 5                                     | 25                                   | 40                                   | 16                                  |
| $u^*_0 \times 10^{-2}$ [m s <sup>-1</sup> ]                               | 1.7 (0.0)                             | 1.3 (0.3)                            | 1.1 (0.6)                            | 0.5 (0.2)                           |
| $\langle w'b' \rangle_0 \times 10^{-9}$ [m <sup>2</sup> s <sup>-3</sup> ] | -8.2 (0.8)                            | -3.3 (2.0)                           | -4.9 (2.6)                           | -2.4 (0.6)                          |

Vertical shear were measured with two airfoil shear probes (PNS-06), at a frequency of 512 Hz. Turbulent dissipation rates,  $\epsilon = 7.5\nu\langle u_z^2 \rangle$ , where  $\nu$  is the kinematic molecular viscosity and  $\langle u_z^2 \rangle$  is the spectral variance of vertical shear of current, were estimated independently from the two shear probes by fitting the measured shear spectra to the empirical Nasmyth spectrum (Nasmyth, 1970; Wolk et al., 2002):  $\Psi = \frac{8.05\xi^{\frac{1}{3}}}{1+(20.6\xi)^{3.715}}$ , where  $\xi = kL_k$  is the cyclic wavenumber as a product of the wavenumber  $k$  and the Kolmogorov length scale  $L_k = \left(\frac{\nu^3}{\epsilon}\right)^{0.25}$ . A reduction factor of 0.4 for the upper limit when using the Kolmogorov length scale is applied, as the measured spectra do not follow the theoretical shape close to the edge of the inertial subrange for low turbulent dissipation rates. The viscosity  $\nu$  is the temperature-dependent and is approximated as  $\nu = (1.792747 - 0.05126103T + 0.0005918645T^2)$  (Cisewski et al., 2008), where  $T$  is the in situ temperature.

To calculate  $\epsilon$ , the timeseries of shear data of each shear sensor was subdivided into half-overlapping 1-s segments. Then, the one-sided power spectrum of shear was calculated using the Bartlett window and a fast Fourier transformation after a linear trend was removed. The final value of  $\epsilon$  is determined as the mean of the two estimates from the two shear probes. For the analysis, the estimates were averaged to 1 m resolution using a second-degree smoothing filter. Data points above 3 m depth, where the probe is typically not in a perfect free-falling, and at low descending speed ( $<0.3$  m s<sup>-1</sup>) were discarded. The lower detection level (noise level) of  $\epsilon$  is about  $8 \times 10^{-10}$  W kg<sup>-1</sup>, which is determined as the mode value of the overall estimates for deeper quiescent layers at  $>50$ m depth.

The diapycnal turbulent fluxes with respect to scalar quantities, that is, heat, salinity and buoyancy, are evaluated by the following formula:  $\langle w'C' \rangle = -K_z \frac{dC}{dz}$ , where  $C$  is the arbitrary scalar variable and  $z$  is the vertical coordinate (pointing upwards). Here, we approximate the diapycnal coordinate as the vertical coordinate,  $z$ . The diapycnal momentum flux is expressed by  $\langle u'w' \rangle = -K_v \frac{d|U_w|}{dz}$ , where  $|U_w| = \sqrt{U_w^2 + V_w^2}$  is the RMS magnitude of the horizontal current. Here, the turbulent diffusivity,  $K_z$ , and the turbulent viscosity,  $A_z$ , are both derived from the MSS-based  $\epsilon$ . Following the relation proposed by Osborn (1980),  $K_z$  is computed as  $K_z = \Gamma\epsilon/N^2$ , where  $\Gamma$  is the mixing efficiency factor which is assumed to be constant as  $\Gamma = 0.2$  (Oakey, 1982).

The buoyancy frequency  $N$  is defined by  $N = \sqrt{\frac{-g}{\rho_0} \frac{d\rho}{dz}}$ , where  $\rho$  is the seawater density derived from the MSS temperature and salinity profiles,  $\rho_0$  the reference density (1,024 kg m<sup>-3</sup>), and  $g$  is the gravitational acceleration (9.81 m s<sup>-2</sup>). To avoid the singularity problem (i.e., division by  $N \sim 0$ ), vertical segments in neutral stratification ( $N < 1$  cycle per hour [cph]) are excluded from the calculation of  $K_z$ . Turbulent diapycnal viscosity,  $A_z$  is derived from the relation  $A_z = \epsilon/(d|U_w|/dz)^2$ , where in the TKE budget the shear production term is assumed to be comparable with the dissipation term, that is,  $\langle u'w' \rangle \frac{d|U_w|}{dz} = -A_z \left(\frac{d|U_w|}{dz}\right)^2 = -\epsilon$  (Thorpe, 2005). Here, the vertical shear of horizontal velocity,  $\frac{d|U_w|}{dz}$ , is derived from the ADCP currents.

#### 2.4. Turbulent Fluxes From Local Turbulence Closure (LTC)

The boundary conditions at the ice–ocean interface greatly influence the turbulence level in the IOBL. Here we incorporate the LTC approach at the interface (McPhee, 2008a) (Figure 4). The heat and salinity balance in the IOBL can be simplified as (McPhee, 1994):

$$\langle w'T' \rangle_0 = \alpha_h(T_w - T_0)u_0^* = w_0Q_L + \dot{q}$$

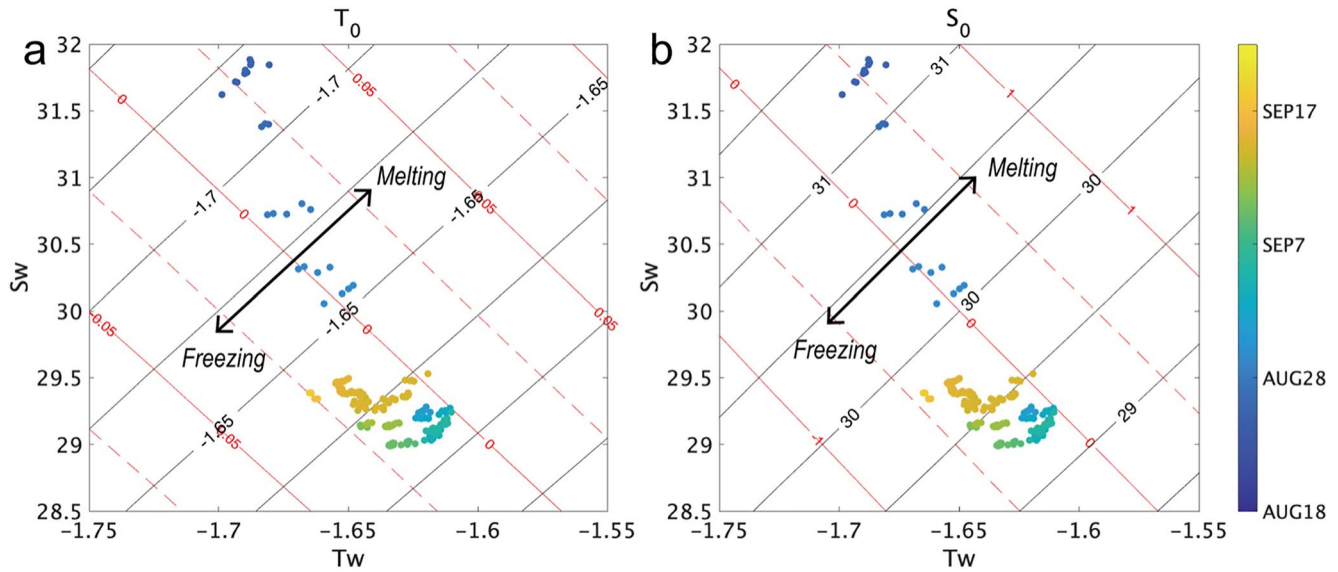


**Figure 4.** Diagram of the solutions of Equation 5 for the interfacial temperature ( $T_0$ ) and salinity ( $S_0$ ) as a function of surface mixed layer (SML)-averaged temperature and salinity, respectively  $T_w$  and  $S_w$ . Contours in black and red, respectively, show the solutions and their changes from the SML-averages. Note that the conductive heat flux is assumed to be negligible (i.e.,  $\dot{q} \approx 0$ ). Ice grows if  $T_w - T_0 < 0$  and  $S_w - S_0 < 0$ , whereas ice melts if  $T_w - T_0 > 0$  and  $S_w - S_0 > 0$ . Colored dots represent observed mean temperature and salinity in the SML, where color denotes the calendar date.

$$\langle w' S' \rangle_0 = \alpha_s (S_w - S_0) u_0^* = -w_0 (S_i - S_0), \quad (3)$$

where  $H$  is the ice thickness and  $dH/dt$  represents the sea ice growth rate,  $S_0$  and  $T_0$  are temperature and salinity at the ice-ocean interface,  $w_0 = \frac{-\rho_{ice}}{\rho_w} \frac{dH}{dt}$  is the isostatically adjusted melt rate,  $\alpha_h$  and  $\alpha_s$  are the turbulent coefficients for heat and salt, respectively. In the present study, considering the double-diffusion favorable circumstance where relatively cold and fresh water lies on top of relatively warm and salty water, we adopt constants of  $\alpha_h = 0.011$  and  $\alpha_s = \alpha_h/50$  (McPhee, 2008a; Sirevaag, 2009), empirically suggested from the power-law relation between molecular diffusivities of heat and salt (Notz et al., 2003). In Equation 3,  $Q_L$  is the latent heat of fusion and is parameterized by  $Q_L = L_f/C_p(1 - 0.03 \times S_i)$ , where  $L_f = 333.5 \text{ kJ kg}^{-1}$  represents the latent heat of pure ice and  $C_p$  is the specific heat of seawater ( $3.99 \times 10^{-3} \text{ J kg K}^{-1}$ ). In addition,  $T_w$  and  $S_w$  denote the far-field temperature and salinity of seawater, respectively, and are assumed to be the averages of those over the SML. The heat and salt fluxes together yield the buoyancy flux in the IOBL through

$$\langle w' b' \rangle_0 = g(\beta_S \langle w' S' \rangle_0 - \beta_T \langle w' T' \rangle_0) \quad (4)$$

where  $\beta_S$  and  $\beta_T$ , respectively, are the haline contraction and thermal expansion factors. Negative values of  $\langle w' b' \rangle_0$  indicate a freezing phase for seawater near the ice-ocean interface, leading to statically unstable convection in the IOBL. Positive values indicate melting of sea ice, strengthening the stratification in the SML. The freezing temperature,  $T_f$ , at the ice-ocean interface is related to  $S_0$  and  $T_0$  by  $T_0 = T_f(S_0) \approx -mS_0$  (Gill, 1982), where  $m = 0.055^\circ\text{C psu}^{-1}$  is defined as the slope of the freezing line on a temperature-salinity diagram. Then, Equation 3 may be re-written in terms of  $S_0$  as

$$mS_0^2 + (T_H + T_L - mS_i)S_0 - T_H S_i - T_L S_w = 0 \quad (5)$$

where  $T_H = T_w - \frac{\dot{q}}{\alpha_h u_0^*}$  and  $T_L = \frac{\alpha_s Q_L}{\alpha_h}$ . In the above equation, the percolation velocity (vertical migration speed of liquid water through sea ice pores) is ignored in the calculations because it is inconsequential (McPhee, 2008a). Based on in situ measurements of sea ice salinities from ice cores, the salinity  $S_i$  is set to 5.0. The conductive heat flux  $\dot{q}$  is derived from the ice mass balance observations as described further below. Consequently, Equation 5 can be further simplified. It yields the solutions for  $S_0$  and  $T_0$  if a pair of  $S_w$  and  $T_w$  is given arbitrarily (Figure 4). Note that if  $\dot{q}$  is negligible, the computations of  $S_0$  and  $T_0$  for Equation 5 are independent of  $u_0^*$ . The magnitude of  $u_0^*$  can affect the rate of the thermodynamic ice growth through the turbulent fluxes according to Equation 3.

2.5. Observation of Ice Temperature and Assessment of Conductive Heat

To quantify the temperature variation within the ice interior, we used data from a SIMBA-type ice mass balance buoy 2020T78 (hereafter referred to as SIMBA: manufactured by SAMS Enterprise, Oban, Scotland). The buoy is equipped with a string of thermistors installed in a drill hole through the ice (Jackson et al., 2013). 240 thermistors were evenly distributed along the 4.8 m string at a constant spacing of 2 cm (Figure 5). The temperature

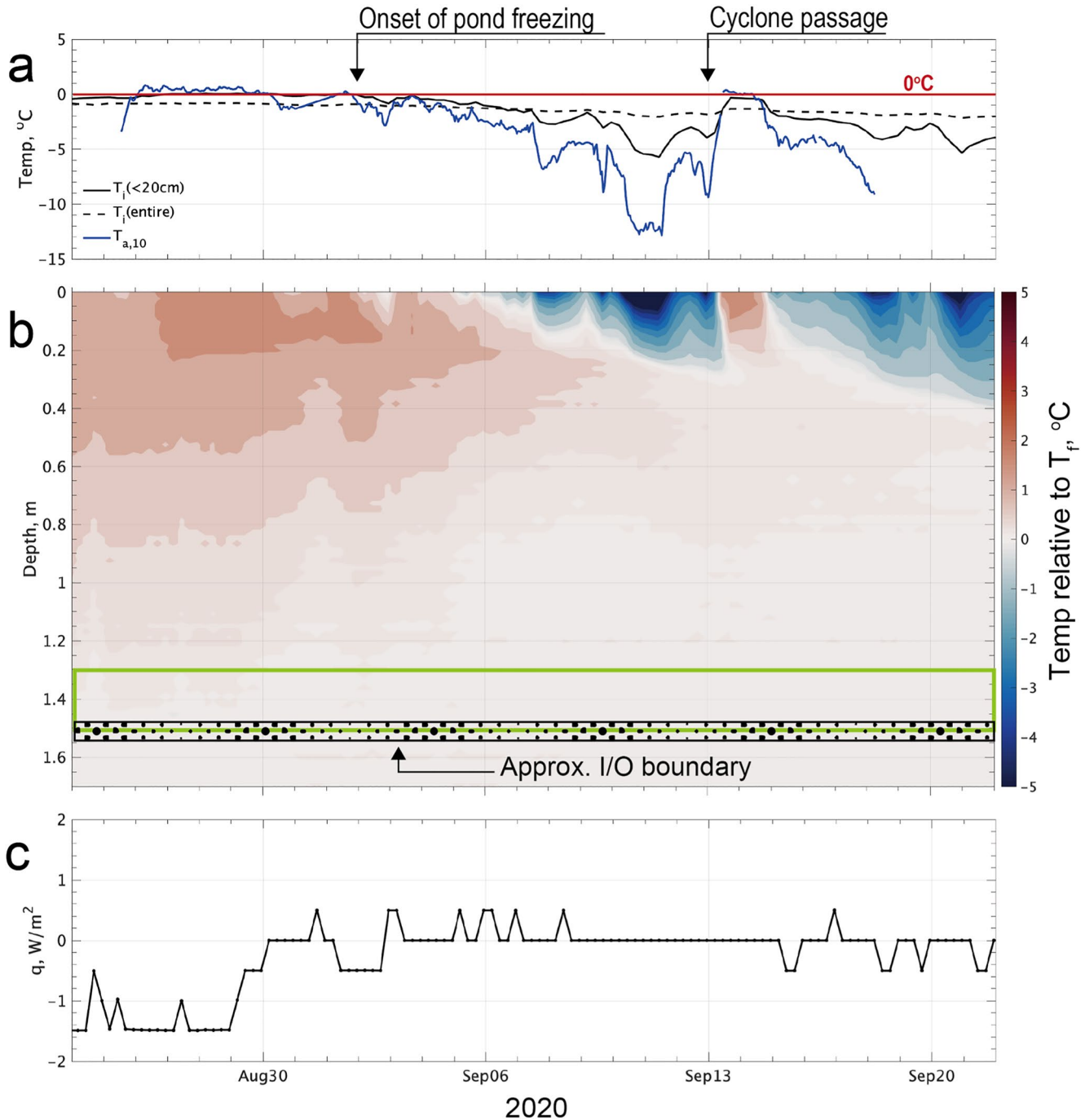


**Figure 5.** (a) Time series of 10-m air temperature  $T_{a,10}$  (blue) and vertical averages of ice interior temperatures  $T_i$  (solid line for depths  $<0.2$  m; dashed line for entire column); (b) contour plot of ice and ocean temperatures relative to the freezing point  $T_f = -1.63^\circ\text{C}$ , where salinity of seawater is assumed to be 30 psu. The hatched horizontal strip indicates the approximate boundary between ice and ocean. (c) Time series of conductive heat  $q$ , which is calculated by Equation 6 with the vertical gradient of  $T_i$ , especially within 0.2 m above the ice bottom (green rectangular). The positive  $q$  indicates upward heat transfer, and vice versa.

measurement accuracy is stated as  $\pm 0.125^\circ\text{C}$ . The SIMBA 2020T78 was deployed on 24 August 2020 in an area of undeformed level ice at site ( $x = 50, y = -20$ ) (Figure 1b) with an initial ice thickness of 1.5 m and without snow cover. The conductive heat flux  $\dot{q}$  through the ice was estimated according to Untersteiner (1961) as

$$\dot{q} = -K_i \frac{dT_i}{dz} / \rho_w C_p \quad (6)$$

where  $T_i$  is the observed ice temperature. Here,  $K_i = K_f + 0.117 \frac{S_i}{T_i}$ , where  $K_f$  is the thermal conductivity for fresh ice ( $2.04 \text{ J m}^{-1} \text{ K}^{-1} \text{ s}^{-1}$ ) and  $S_i$  is 5.0. For our study, we focus on the conductive heat flux through a layer at the bottom of the ice. Therefore, we only used temperature readings of the lowermost 10 thermistors (spanning 20 cm) that were still in the ice (green box in Figure 5b).

## 2.6. Mixed-Layer Slab Model

The energetic inertial motion in the ice drift is expected to transfer great amounts of momentum and kinetic energy into the SML. We use a mixed-layer slab model to demonstrate the prediction of the inertial oscillation in the SML, which results in the periodic ice drift. The model is based on the balance of inertial kinetic energy over the SML (e.g., D'Asaro, 1985; Pollard & Millard, 1970). Vertically averaged motion in the SML is assumed to be forced by surface stress,  $\mathbf{T} = \frac{\tau_x + i\tau_y}{\rho}$ , and decelerated by friction as

$$\frac{d|\frac{1}{2}\mathbf{Z}_I|^2}{dt} = -r|\mathbf{Z}_I|^2 - \Pi \quad (7)$$

The kinetic energy flux from the ice drift to the underlying surface water is expressed as  $\Pi$ :

$$\Pi = \text{Re} \left[ \frac{\mathbf{Z}_I}{\omega^* D_{ML}} \frac{d\mathbf{T}^*}{dt} \right] \quad (8)$$

where  $\mathbf{Z}_I = u + iv$  is the complex form of the SML depth-mean current,  $u$  and  $v$ , respectively, represent the zonal and meridional components, the frequency  $\omega$  is given as  $\omega = r + if$ . In the equation,  $\omega^*$  is the complex conjugate of the frequency given by  $\omega = r - if$ , while  $\mathbf{T}^*$  is the one of the surface stress given by  $\mathbf{T}^* = \frac{\tau_x - i\tau_y}{\rho}$ . The SML thickness  $D_{ML}$  is assumed to be constant (20 m). Here,  $r$  represents an artificial damping rate of 3.5 d. The choice of parameters does not alter our scientific results and conclusions when considered for realistic ranges ( $r = 2-4$  d;  $D_{ML} = 15-25$  m). The computation proceeds at 1 hr temporal resolution, with explicit forcing based on the observed ice drift. For our calculations, the surface momentum flux reflects the currents based on the previous time step. Consequently, the ice-ocean momentum exchange is  $\tau_x + i\tau_y = \rho C_w |\mathbf{Z}_I - \mathbf{U}_i| (\mathbf{Z}_I - \mathbf{U}_i)$ , where  $\mathbf{U}_i$  is the observed ice velocity in a complex form and  $C_w$  is the ice-ocean drag coefficient.

In the calculation, we adopted  $C_w = 3.0 \times 10^{-3}$  (Shirasawa & Ingram, 1997) for the default setting. According to the past Arctic expeditions,  $C_w$  varies typically in the range of  $2-5 \times 10^{-3}$  (e.g., Leppäranta, 2005; Shirasawa, 1986), depending on various environmental factors: ice type, ridging density, keel depth, and so on. The different choices between  $C_w = 2-5 \times 10^{-3}$  exhibited a  $\sim 15\%$  variation in the predicted amplitude (measured as a standard deviation) of  $\mathbf{Z}_I$ .

## 2.7. Meteorological Observations

We used wind speed and air temperature measured at 10-min intervals at 10 m height on the meteorological and flux tower that was located at ( $x = -350, y = -250$ ) outside the frame of Figure 1b. The data, shown in Figure 2a, were interpolated onto an hourly grid before the analysis. More detailed information about the meteorological instruments and the data processing are available in Cox et al. (2021).

## 3. Environmental Properties

### 3.1. Atmospheric Conditions

During the observational period in the late summer months, near-surface atmospheric conditions were characterized by relatively high air temperature and frequent storm events crossing over the drift trajectory (Figure 2a; Rinke et al., 2020). According to the ERA5 reanalysis, the 10-m temperature has been anomalously high for the

past four decades (Rinke et al., 2020). From the in situ measurements taken from 28 August to 19 September, the mean  $T_{a,10}$  was  $-4.0$  with a standard deviation of  $3.2^{\circ}\text{C}$  (black curve in Figure 2a). During 10–11 September, an air temperature minimum ( $T_{a,10} < -10^{\circ}\text{C}$ ) occurred. The mean wind speed was  $5.6$  with a standard deviation of  $2.7\text{ m s}^{-1}$ . Strong winds exceeding  $10\text{ m s}^{-1}$  were observed during two storm events on 6 September and 13–14 September (red curve in Figure 2a).

### 3.2. Sea Ice Conditions

#### 3.2.1. Thermodynamic Evolution of Sea Ice

The ice interior temperatures measured by the SIMBA illustrate the spatiotemporal evolution of the heat budget during the 1-month observational period (Figure 5). Again, there was no snow layer near the site of SIMBA measurement, but it was covered by melt ponds everywhere in the neighborhood. In the first half of this period, the data showed ice interior averaged temperatures of  $\sim -1$  and  $\sim 0^{\circ}\text{C}$  for the entire ice column and upper  $0.2\text{ m}$ , respectively (Figure 5a). This was warmer than the freezing point of the near-surface sea water,  $T_f \approx -1.6^{\circ}\text{C}$  (Figure 5b). The positive temperature anomaly relative to  $T_f$  changed to a negative anomaly within the top  $0.3\text{ m}$  after September 6 (see also Figure 5b). At the site, the researchers observed with their eyes that the fresh water in surface melt ponds began to refreeze around September 2. The cooling trend in the upper ice column was interrupted by the passage of a low-pressure system around September 13–14, which brought warmer air temperatures  $T_{a,10} > 0^{\circ}\text{C}$  to the region. Being sufficiently isolated from this surface forcing, temperatures in the lower part of the ice column ( $>0.5\text{ m}$ ) showed only slight changes in temperatures relative to seawater (see a green rectangular in Figure 5b). As a result, heat conduction through the ice was negative (oriented toward the ocean) until the end of August, and estimated as  $\dot{q} = -1.5\text{ W m}^{-2}$ . Between early September and the end of the observational period,  $\dot{q}$  remained close to zero (Figure 5c).

According to earlier studies based on ice mass balance observations in the Arctic, the onset of basal freezing typically occurs between October and December (e.g., Lei et al., 2018). For the freezing regime, it is known that the conductive heat is transported upward and significantly influences the heat balance near the ice bottom. Our SIMBA observations (Figure 5) further indicates that the termination of the melting regime (i.e., ending of negative  $\dot{q}$ ) toward a preconditioning stage (i.e., near-zero  $\dot{q}$ ) for consequent basal freezing.

#### 3.2.2. Sea Ice Dynamics

Sea ice drift was generally energetic during the study period, which was in the transition from near-free drift to a more consolidated ice pack after the summer sea ice concentration minimum (e.g., Kawaguchi et al., 2012). The ice floe drifted east toward the geographic North Pole prior to 8 and 9 September, then the floe moved southwest toward the Fram Strait (Figure 1a). On average, the ice drift was typically  $0.2\text{ m s}^{-1}$  or less. The fastest ice drift during the study period of  $\sim 0.4\text{ m s}^{-1}$  ( $35\text{ km d}^{-1}$ ) was directed northwards and recorded around 13 and 14 September, resulting from a passing cyclone (Figure 2b).

From the ice drift, the magnitude of computed interfacial friction velocity  $u_0^* = |u_0^*|$ , assuming roughness  $z_0 = 0.01\text{ m}$  (see Section 2.1 and Equation 1), shows the mean value of  $6.5 \times 10^{-3}\text{ m s}^{-1}$  with a standard deviation of  $3.6 \times 10^{-3}\text{ m s}^{-1}$  (Figures 2b and 2c). It is noteworthy that  $u_0^*$  reached the greatest magnitude of nearly  $1.9\text{ cm s}^{-1}$  on September 13–14. The storm event caused apparent semi-diurnal fluctuations in both ice drift and  $u_0^*$  (Figures 2b and 2c).

The 10-m wind speed and ice drift speed, low-passed with a 24 hr Butterworth filter, were closely correlated ( $R = 0.85$ ) (Figure 6a). In the scatter diagram, the ice drift speed is mostly distributed between the slopes of 2%–4% relative to the 10-m wind, with a best-fit line of 2.9%. Earlier studies found that the ice drift can follow near-surface winds at an approximate ratio of 3% in the absence of resistance to internal ice stress (Leppäranta, 2005; Zubov, 1945).

The magnitude of sea ice drift is also highly correlated with the subinertial current at 10 m depth in the IOBL-adjusted coordinate, where  $R = 0.87$  (Figure 6b). Statically, the sea ice drift is slightly faster than the 10-m depth current by a factor of 1.3. This suggests that the sea ice motion generally adds momentum into the underlying sea water and therefore drives the movement there.

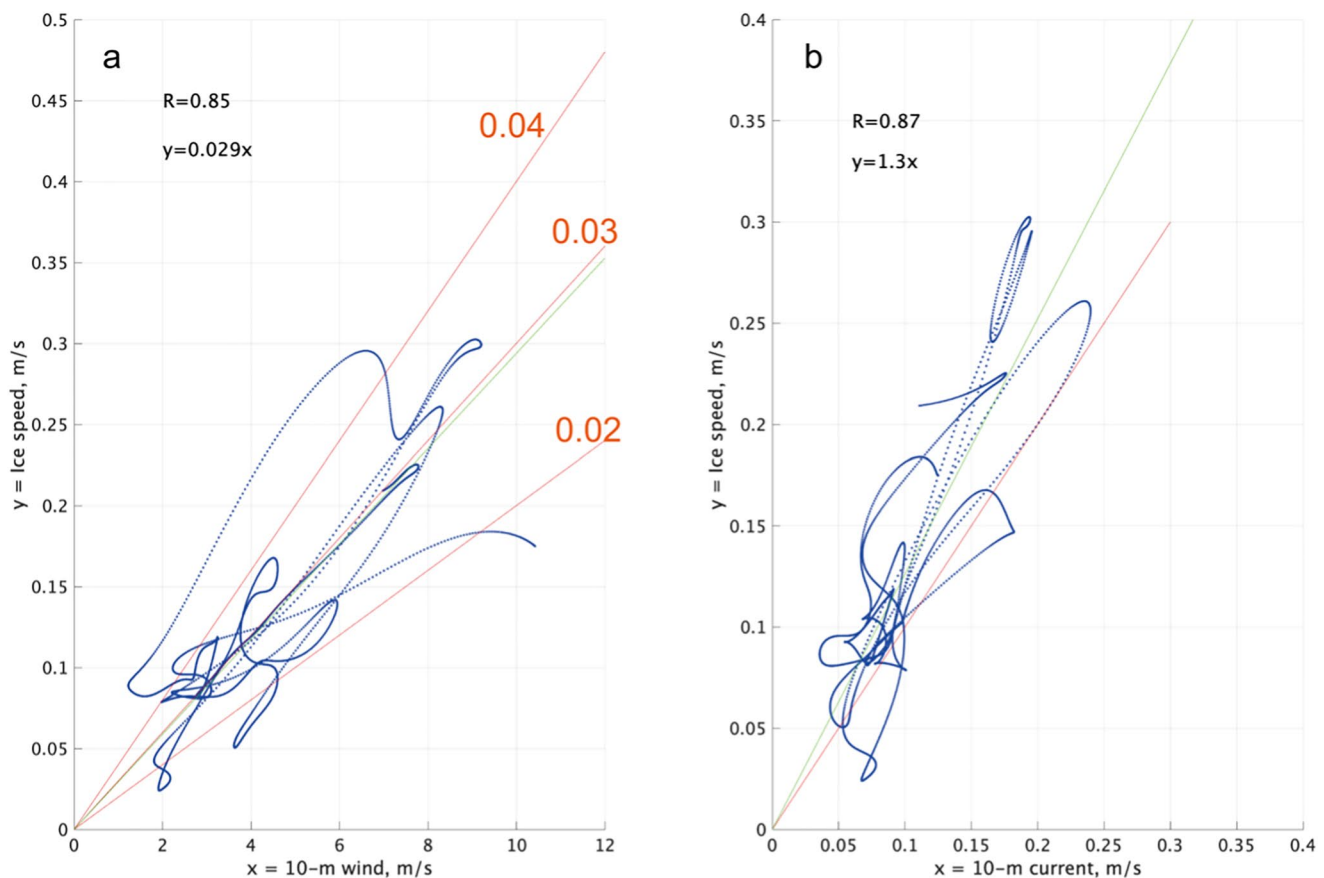


**Figure 6.** Scatter plots of mean amplitude of sea ice drift velocity versus (a) 10-m height wind and (b) 10-m depth current in the ice–ocean boundary layer-adjusted coordinate. Velocities are low-pass filtered using a 24 hr Butterworth filter. In (a), the best-fit regression is shown by the green line. Nominal ratios of 0.02, 0.03, and 0.04 are shown by red lines. In (b), a regression line is drawn in green; a slope of  $U_i = U_w$  is in red. Correlation coefficients,  $R$ , and the formula of linear regression are indicated in each panel.

In the high frequency domain of the ice drift, the most energetic part is found in the clockwise (CW) rotation (Figures 2b and 3a). This result indicates that the inertial oscillation, which is driven primarily by surface winds, should dominate the ice movement. The inertial periodicity (11.97 hr at 89.0°N) of the ice drift is clearly revealed by the wavelet analysis of the horizontal ice motion deconvolved into CW and anticlockwise rotational components (Figure 7). The spectrum shows the dominance of the semidiurnal frequency of around 2 cpd in the CW rotational direction rather than in the counterclockwise (CCW) counterpart. Statistically significant energy in the CW wave spectra was intermittently observed during 13–24 September, following the passage of the cyclone.

### 3.3. Water Mass Properties

The MSS observations revealed the hydrographic properties of the upper part of the water column (Figure 8). Similar to previous reports (e.g., Aagaard et al., 1981; Morison et al., 1998; Rudels et al., 1996), the upper ocean consists of three distinct segments: the SML, the cold halocline layer (CHL), and the intermediate-depth Atlantic Water (AW) layer (Figure 8b). As a whole, the SML is characterized by an extremely weak stratification of  $N = 4.0 \pm 3.5$  cph, where  $T$  and  $S$  are nearly homogeneous and typically characterized by  $T = -1.65 \pm 0.05^\circ\text{C}$  and  $S = 29.7 \pm 1.0$ , respectively (Table 2). Near the SML base,  $N$  reaches its maximum of  $23.5 \pm 5.6$  cph (Table 2; Figure 8c). In the CHL, which lies below the SML, the water temperature remains nearly constant around  $-1.8^\circ\text{C}$ , so that the large salinity gradient largely determines the density stratification. The SML and the CHL insulate the underlying AW layer from the surface forcing (Carmack, 2000).

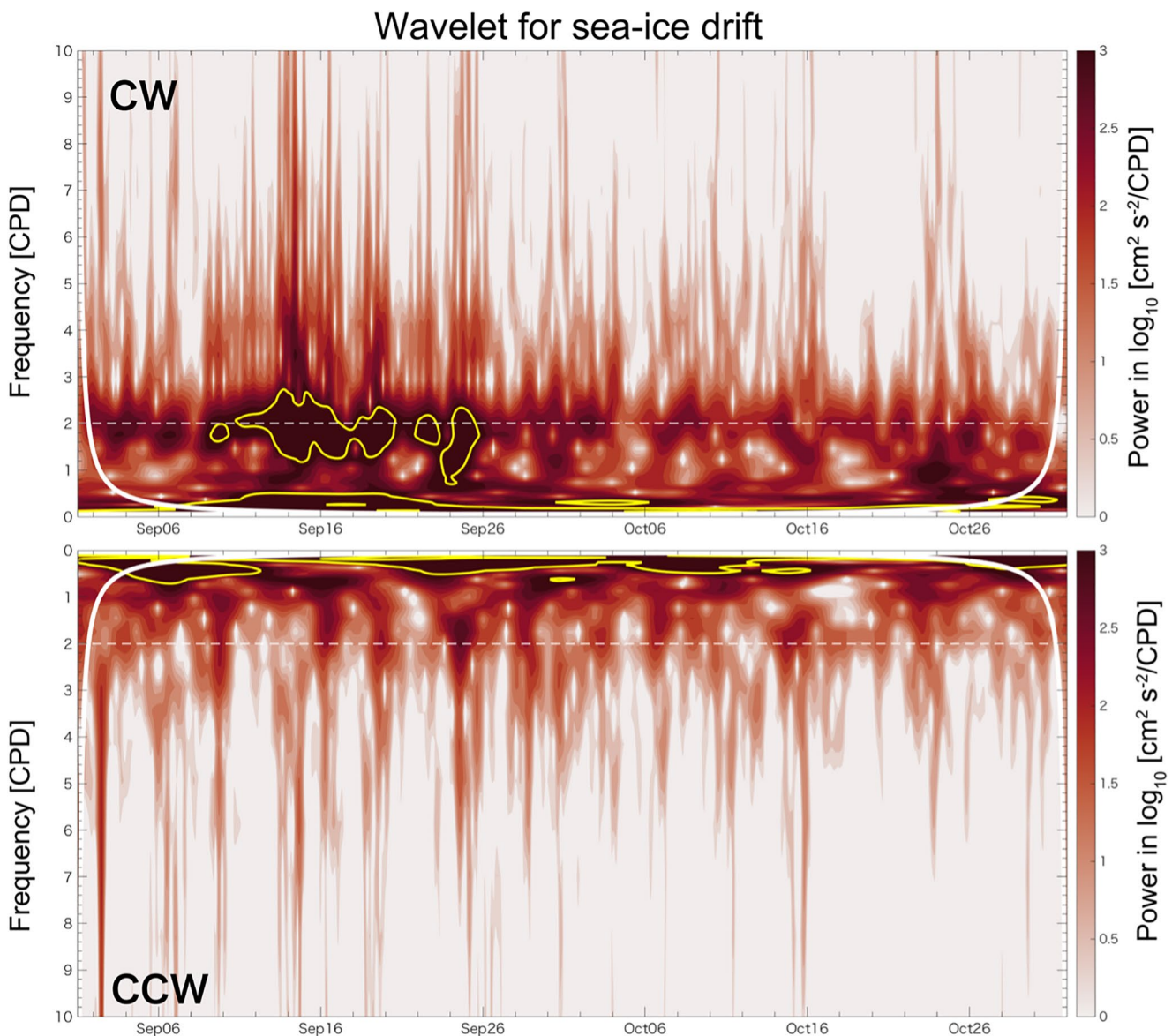


**Figure 7.** Results from Morlet wavelet analysis of sea ice drift. The upper and lower sections respectively represent clockwise (CW) and counterclockwise (CCW) rotations. A region of 95% confidence is encircled by yellow solid curves, while the cone of influence (COI) is by bold white curves. Note that the time axis is extended through the end of October for accentuation of the enhanced oscillation in September.

During 27–29 August, an increase of  $T$  from  $-1.68^{\circ}\text{C}$  to  $-1.62^{\circ}\text{C}$  was observed in the SML, accompanied by a decrease in  $S$  from 31.5 to 29.0 psu (Figures 4 and 9). The abrupt freshening of the SML suggests that the ice floe moved across a surface frontal structure, subsequently entering a region where fresh meltwater ( $S < 29$  psu) prevailed in the SML. Assuming that the melt water is uniformly mixed over the 18.4 m thick SML (Table 2), a drop of 2–2.5 in the SML-averaged salinity,  $S_w$ , corresponds to a melt of 1.4–1.8 m ice thickness. The freshening in the SML can also raise the freezing temperature  $T_f$  in the same layer. We will argue how the change of the observed thermohaline properties in the SML can influence the thermodynamic condition at the interfacial boundary as well as the growth and melt rate at the ice bottom. This issue is addressed in Section 3.4.

For this study, we define the depth of the SML ( $D_{\text{ML}}$ ) as the shallowest depth where an increment of seawater density relative to the surface density exceeds  $0.25 \text{ kg m}^{-3}$  (Toole et al., 2010). Throughout the observational period, fluctuations of  $D_{\text{ML}}$  were small, with a mean of 18.4 m and a standard deviation of 3.1 m (magenta triangles in Figure 9; Table 3).

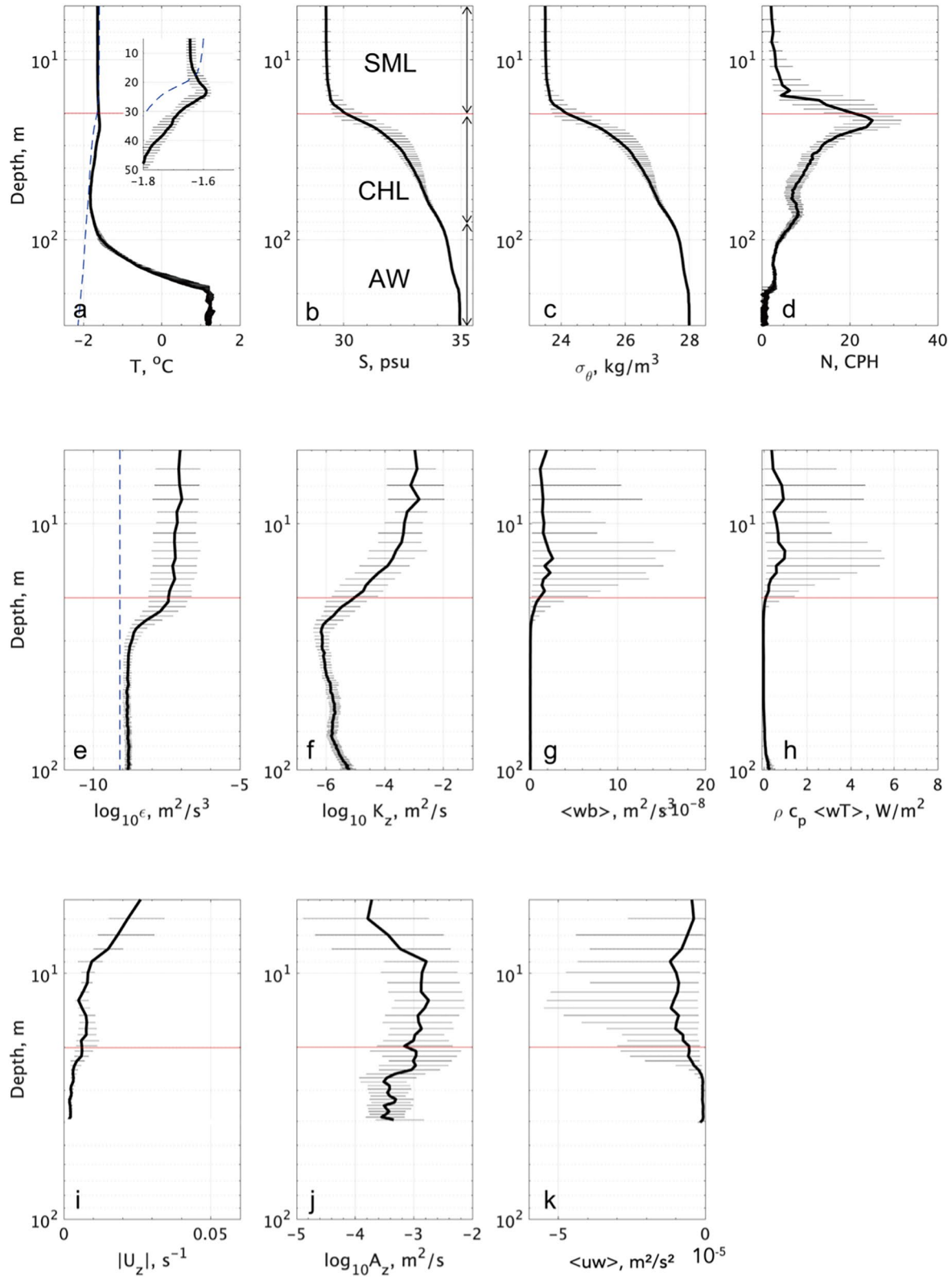


Figure 8.

**Table 2**

Summary of Turbulence-Related Variables, With Medians and Interquartile Range (Differences Between First and Third Quartiles) for Depth Ranges of  $0.2 \leq |z|/D_{ML} \leq 0.9$  and  $0.9 < |z|/D_{ML} < 1.1$

| Variables   | $0.2 \leq  z /D_{ML} \leq 0.9$ | $0.9 <  z /D_{ML} < 1.1$ |
|---|--------------------------------|--------------------------|
| $T$ [°C]  | -1.65 (0.05)                   | -1.64 (0.04)             |
| $S$ [psu]   | 29.7 (1.1)                     | 29.9 (1.1)               |
| $N$ [cph]   | 3.5 (2.5)                      | 23.5 (5.6)               |
| $U_z \times 10^{-3}$ [s <sup>-1</sup> ]                                 | 9.0 (4.1)                      | 9.3 (6.3)                |
| $\epsilon \times 10^{-8}$ [m <sup>2</sup> s <sup>-3</sup> ]             | 6.3 (34.1)                     | 8.8 (24.3)               |
| $K_z \times 10^{-5}$ [m <sup>2</sup> s <sup>-1</sup> ]                  | 32 (161)                       | 1.2 (3.6)                |
| $A_z \times 10^{-4}$ [m <sup>2</sup> s <sup>-1</sup> ]                  | 9.8 (35.7)                     | 13.6 (48.0)              |
| $\langle w'b' \rangle \times 10^{-8}$ [m <sup>2</sup> s <sup>-3</sup> ] | 1.5 (9.5)                      | 1.8 (5.3)                |
| $\rho C_p \langle w'T' \rangle$ [W m <sup>-2</sup> ]                    | 0.62 (3.2)                     | 0.34 (1.0)               |
| $\langle u'u' \rangle \times 10^{-6}$ [m <sup>2</sup> s <sup>-2</sup> ] | -7.4 (34.0)                    | -12.3 (31.0)             |

Note. For  $T$ ,  $S$ , and  $N$ , values are the averages and standard deviations.

### 3.4. Boundary Fluxes Based on LTC

The analysis of the boundary flux solutions (Figure 4) suggests that the thermohaline properties of the SML drastically changed and simultaneously crossed the critical curves of  $T_w - T_0 = 0$  and  $S_w - S_0 = 0$  as the ice moved with the wind forcing (see red contours for the residuals). The solutions in Figure 4 indicate that a phase of basal melt shifted to the refreezing phase at the bottom of the ice (see Equation 3). The estimate of the boundary fluxes reveals that the growth rate ( $dH/dt$ ) transitions from negative (melting of ice) to positive (growing of ice) at the end of August (Figure 10). The largest ice growth rate was observed during the cyclone event on 14 September (Figure 10a), with episodic peaks of 0.2–0.5 cm d<sup>-1</sup> for a few days. For the entire study period,  $dH/dt$  was on average 0.13 cm d<sup>-1</sup> with the standard deviation of 0.15 cm d<sup>-1</sup> (Table 4).

On the interfacial boundary, the turbulent heat flux turns from positive to negative, that is, from gaining to losing heat, reaching 15 W m<sup>-2</sup> during the storm event (Figure 10c). The mean heat flux  $\rho C_p \langle w'T' \rangle_0$  during the study period was about -3.8 W m<sup>-2</sup> with a standard deviation of 4.6 W m<sup>-2</sup> (Table 4), with similar patterns for the salinity and buoyancy fluxes; the turbulent fluxes changed sign from positive to negative in early September (Figures 10b and 10d). The positive buoyancy flux resulted from the stabilization of the IOBL in August, and it shifted to negative when ice growth began in early September. The negative value of  $\langle w'b' \rangle_0$  was on the order of

$10^{-9}$  m<sup>2</sup> s<sup>-3</sup>, which is two orders of magnitude less than those in the mid-winter (cf.  $\langle w'b' \rangle_0 = -0.7 \times 10^{-7}$  m<sup>2</sup> s<sup>-3</sup> in a freezing lead in McPhee and Stanton (1996)).

We assess the relative contributions between the shear and buoyancy terms in the steady-state TKE balance, that is,  $P_{sh} + P_b - \epsilon \approx 0$ , where  $P_{sh}$  and  $P_b$  are the shear- and buoyancy-driven production terms. Thus, we computed the Obukhov length,  $L_O$ , based on the surface LTC fluxes above, where  $L_O$  is given by  $L_O = \frac{u_*^3}{\kappa \langle w'b' \rangle_0}$  (Obukhov, 1971), where  $\kappa$  is 0.4. Our computations yield mean values of  $|L_O| = 844$  m but with a higher standard deviation of 1,541 m (Table 3), suggesting the boundary layer fluctuating between the stable and unstable states during the study period.

Here, we introduce the non-dimensional number,  $I_O = L_O/D_{ML}$  (Lozovatsky et al., 2005). Timeseries of the hydrography indicated that  $I_O$  largely shifted from positive (red dots, Figure 9b) to negative (blue dots, Figure 9b) values at the end of August, indicating the regime at the ice-ocean boundary interface that changes from stable (melting with positive  $I_O$  values) to unstable (refreezing with negative  $I_O$  values) due to the raising  $T_f$  resulted from intrusion of freshened surface water.

In Section 5, the estimated  $L_O$  will be also used for the evaluation of mixing length,  $\lambda_{LTC}$ , based on the LTC theory, and consequently the shear production of  $P_{sh}(z) = \frac{u_*^3}{\lambda_{LTC}}$  at an arbitrary depth.

## 4. Impacts of Near-Inertial Internal Waves (NIW) to Turbulence

### 4.1. Generation of NIW

Vertical shear of the horizontal current reveals the occurrence of internal wave propagation (Figure 11; see also Figures 3a and 3b). It appears that the iso-phase lines of shear are inclined at a certain angle from the level surface, implying the vertical propagation of internal waves (Leaman & Sanford, 1975). In this sense, we can see the downward-propagating NIWs (i.e., upward in phase propagation) following the storm event during 13–14 September. Vertical phase propagation is about 26 m d<sup>-1</sup> (hypotenuse of yellow triangles in right panels

**Figure 8.** Vertical profiles of (a) temperature  $T$ , (b) salinity  $S$ , (c) potential density anomaly  $\sigma_\theta$ , (d) buoyancy frequency  $N$ , (e) dissipation rate  $\epsilon$ , (f) diffusivity  $K_z$ , (g) buoyancy flux  $\langle w'b' \rangle$ , (h) heat flux  $\rho C_p \langle w'T' \rangle$ , (i) magnitude of vertical shear of horizontal current  $U_z$  (j) viscosity  $A_z$ , and (k) momentum flux  $\langle u'u' \rangle$ , where  $\epsilon$ ,  $K_z$ , and  $A_z$  are shown on a logarithmic scale. In (a), a blue dashed curve shows the freezing temperature,  $T_f$ , while in (e) it shows a noise floor. Red lines show an approximate SML depth. Solid black curves show medians at each level, with thin horizontal lines for a range from first to third quartiles. In (b), vertical segments of distinct water masses are indicated by vertical arrows: SML, cold halocline layer (CHL), and Atlantic Water (AW). Note that the vertical axis is logarithmically scaled.

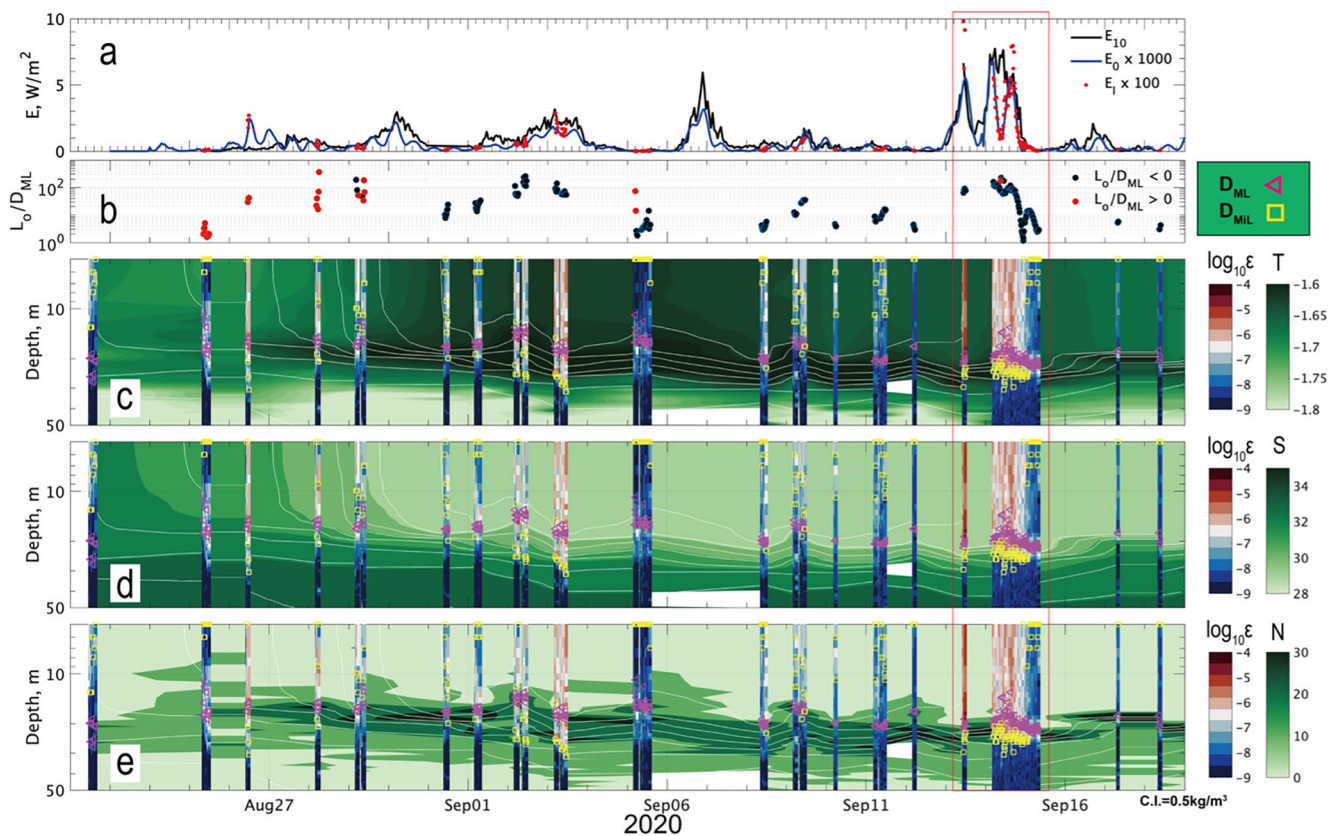


**Figure 9.** Timeseries of microstructure and hydrographic observations: (a) surface mixed layer (SML)-integrated  $\epsilon_p$ , wind work  $E_{10}$ , and under-ice energy flux  $E_0$ , (b)  $D_{ML}$ -normalized Obukhov length  $\frac{L_0}{D_{ML}}$  (c-e)  $T$ ,  $S$  and  $N$  in background shading, overlain with  $\epsilon$  by colored dots. Yellow squares and magenta triangles show the depths of the mixed layer ( $D_{ML}$ ) and the mixing layer ( $D_{MiL}$ ), respectively. The period outlined by red represents the storm event (see Figure 16). Note: in (c-e) the vertical axis is logarithmically scaled. In (c and d), contours and color shades are interpolated with a cubic spline technique of MATLAB®.

of Figure 11). We adopt this value as the estimated vertical phase speed,  $C_z$ . A rough estimate of the vertical wavenumber  $k_z$  is estimated as 0.039 cycles per meter (cpm) (equivalent to 13 m in wavelength) by using  $C_z = \frac{\omega}{k_z}$ , where  $\omega$  denotes the wave frequency and roughly 2.0 cycles per day. Note that the vertical wavelength is likely to vary depending on the local stratification as it travels deeper into the water column (Gill, 1982).

Vertical velocity from the ADCP measurements exhibited noticeable fluctuated perturbations throughout the SML during the specific storm events around 2 and 3 September and 13 and 14 September (Figure 3c). We hypothesize that the fluctuating vertical motion in the SML was produced by the inertial horizontal motion that alternately climbed and descended steep slopes associated with keels of the deformed sea ice (Figure 1b) (e.g., Skillingstad et al., 2003). The vertical displacement was likely to initiate the gravity waves in the weakly stratified water at the lower SML, which exhibited the most favorable oscillation frequency for the propagation.

In general, internal waves should not exist inside the SML, which is believed to be well mixed and/or weakly stratified (e.g., Gill, 1982). However, we found coherent signals of NIWs in the lower part of the SML (right panels in Figure 11), particularly within the depth range between where  $N = 7$  cph (dashed line) and  $\sigma_\theta \sim 25.0$ . This result implies that the NIWs are traveling in the relatively weak stratification in the lower SML, which is presumably constructed as a result of accumulation and re-stratification of the summertime melt water. The waves' signatures were still detectable in the shear data until September 17, almost 3 days after the storm event (Figure 11).

**Table 3**  
Overview of Characteristic Length Scales

| Characteristic length [m]         | Mean (std.) |
|-----------------------------------|-------------|
| Depth of mixed layer, $D_{ML}$    | 18.4 (3.1)  |
| Depth of mixing layer, $D_{MiL}$  | 17.8 (8.1)  |
| Ekman layer thickness, $\delta_E$ | 2.7 (3.1)   |
| Obukhov length magnitude, $ L_0 $ | 844 (1,541) |
| Mixing length, $\lambda_{LTC}$    | 1.3 (0.75)  |

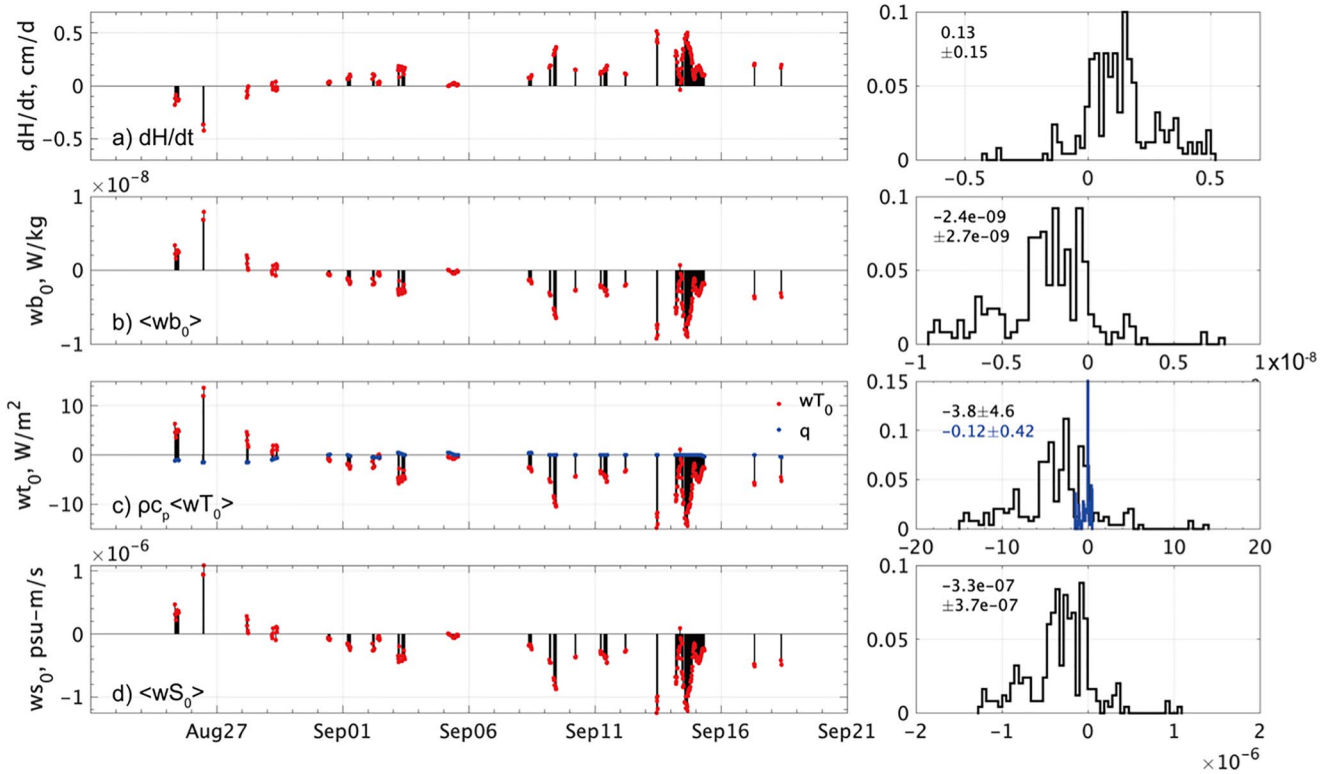


**Figure 10.** Time series of boundary fluxes: (a) growth rate of ice thickness  $\frac{dH}{dt}$ , (b) buoyancy flux  $\langle w'b' \rangle_0$ , (c) heat flux  $\rho C_p \langle w'T' \rangle_0$ , and (d) salt flux  $\langle w'S' \rangle_0$ . In (c), the conductive heat  $q$  is shown by blue dots. In the panels to the right, histograms for the entire period are shown with an average  $\pm$  standard deviation, where vertical axis is the relative frequency.

The near-inertial motions are also detected in the spectral calculation of the horizontal component of the ADCP-measured horizontal current displayed in the IOBL-adjusted coordinate (Figures 3a and 3b). In Figure 12, we show the rotary spectrum for three different depths of 5, 15, and 25 m, respectively representing upper and lower part of SML and the pycnocline (see also Figure 3). We also note that the depth of 5 m is roughly similar to an average of the sea ice draft, which experienced deformation events, near the ADCP location (Figure 1b).

A notable point is that the maximum near  $f$  is significant at the depths of 15 and 25 m, particularly in terms of the CW rotational component. In more detail, the distinct peak for the lower SML (15 m) is rather intensive within a narrow range of frequencies around  $\omega = f$ . It is likely that the near-inertial energy in CW rotation is mainly due to the horizontal motion of the inertial oscillation that is dominant over the SML (further addressed in Section 4.2). At same time, an excess of  $\sim f$  kinetic energy should be partly subject to the influences of the NIW that propagates through the local stratification resulted from the melt water accumulation (Figure 11).

In the meantime, the  $\sim f$  peak at the pycnocline depth is comparatively wider spreading at the frequencies of  $\omega = f-1.3f$  (Figure 12). The spectral curve appears to follow the canonical spectrum for the internal gravity waves (Garrett & Munk, 1975) at a range of 0.1–0.2 cph, corresponding to 1.1–2.4 $f$  (Figure 12). It is thus noteworthy that the kinetic energy elevation at the superinertial frequencies supports the accommodation of NIW packets that can propagate through the stratified water near the pycnocline (Figure 11).

**Table 4**  
*Statistics of Turbulent Fluxes and Related Variables at the Ice–Ocean Interface: Medians and Interquartile Ranges in Parenthesis*

| $u_*^0 \times 10^{-2}$ [m s <sup>-1</sup> ] | $dH/dt$ [cm/d] | $\rho C_p \langle w'T' \rangle_0$ [W m <sup>-2</sup> ] | $q$ [W m <sup>-2</sup> ] | $\langle w'S' \rangle_0 \times 10^{-7}$ [m s <sup>-1</sup> ] | $\langle w'b' \rangle_0 \times 10^{-9}$ [m <sup>2</sup> s <sup>-3</sup> ] |
|---|----------------|--|--------------------------|--|---|
| 0.64 (0.69)                                 | 0.13 (0.15)    | −3.8 (4.6)   | −0.12 (0.42)             | −3.3 (3.7)   | −2.4 (2.7)  |

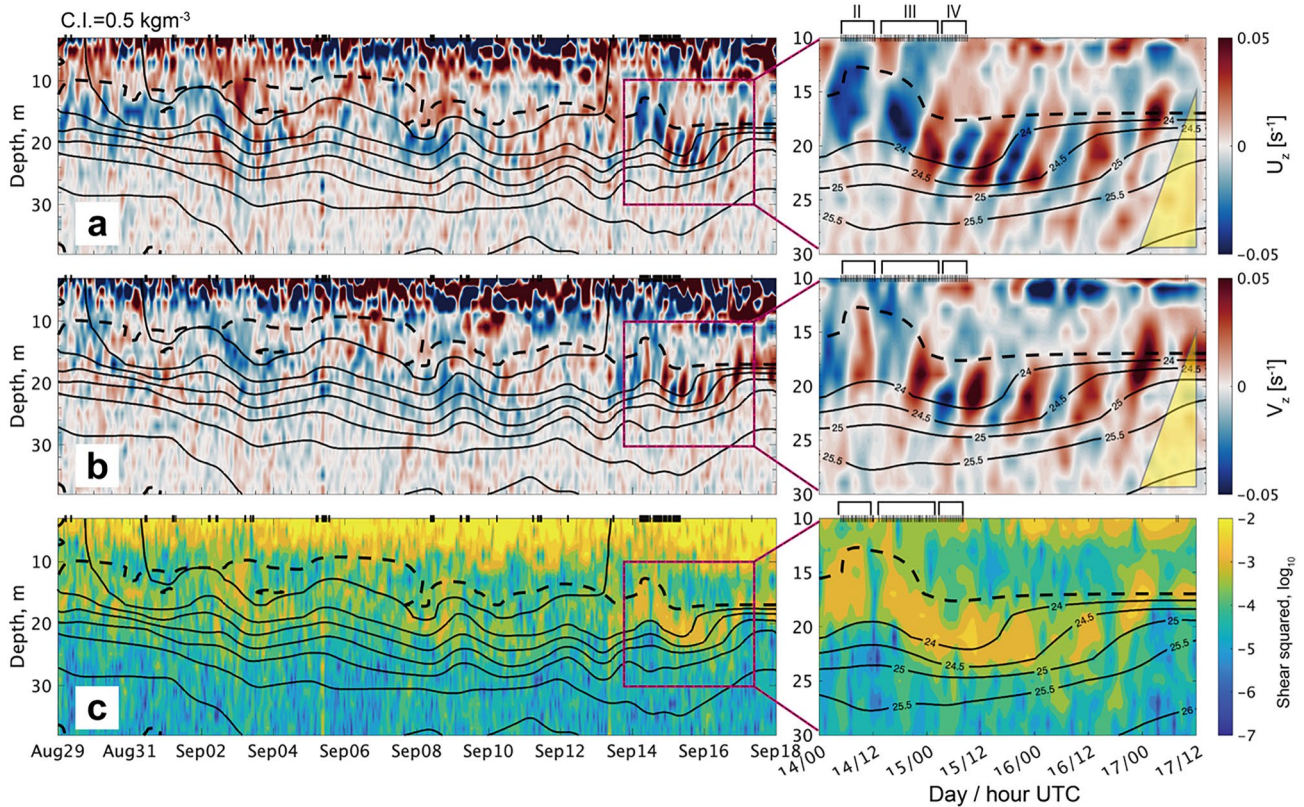


**Figure 11.** Time-vertical sections of vertical shear of (a) zonal and (b) meridional horizontal velocity and (c) sum of shear squared represented on a logarithmic scale. Black contours show the isopycnals based on the MSS measurements, with an interval of  $0.5 \text{ kg m}^{-3}$ . In right panels, close-up views of a storm-induced NIW event is shown. A yellow triangle indicates an approximate slope of  $C_z = 26 \text{ m/d}$  in vertical phase speed, equivalent to a vertical wavelength of  $\lambda_z = 13 \text{ m}$ . Contours of the density field are drawn using a cubic spline interpolation, where the timing of MSS measurements is indicated by (+) at the top of each panel. Black, dashed curves show an isoline of  $N = 7 \text{ cph}$ . Labels (II, III and IV) at top of the right panel show the subsegments for the storm event in mid-September (see also Table 1 for the details).

In addition, we can also find a modest near-inertial peak at a depth of the upper SML (5 m) (at top of Figure 12), while there is an enormous spectral energy over the broad frequencies (cf. the GM level). Unlike the other two depths, the  $\sim f$  peak at 5 m is uniquely characterized by the both rotational components of CW and CCW. Regarding this property, we deduce that the inertial oscillation that shows only the CW oscillation cannot be sufficiently developed within the average depth of the ice keels.

#### 4.2. Inertial Oscillations Predicted by a Mixed-Layer Slab Model

The prediction from the slab model well accounts for the occurrence of inertial oscillation in the mixed layer as a response to the ice drift (Figure 13c; 3). According to the slab model calculation, we find that there are two events during 6–7 September and 13–14 September that contribute momentum input to the SML (Figure 13a). The former inputs only relatively small amounts of kinetic energy into the SML, on the order of  $1.0 \text{ mW m}^{-2}$  or less, so that the resulting inertial oscillation was only weak (Figure 13c). In contrast, the latter delivered much larger amounts ( $>10 \text{ mW m}^{-2}$ ) of near-inertial energy into the SML (Figure 13b), resulting in substantial inertial oscillations with magnitudes of  $10 \text{ cm s}^{-1}$  (Figure 13c). From the comparison of the oscillatory motions between the slab model and the ADCP observation, we notice that the selection of  $C_w = 3.0 \times 10^{-3}$  yields a good agreement with each other. We also infer that the larger inertial response during the second wind event was induced by the longer-lasting strong wind forcing and the consequent ice drift (Figure 2), which lasted for a couple of days (nearly four times the local inertial period). This forced the resonant growth of the inertial oscillation in the surface water (e.g., Kawaguchi et al., 2016; Martini et al., 2014).

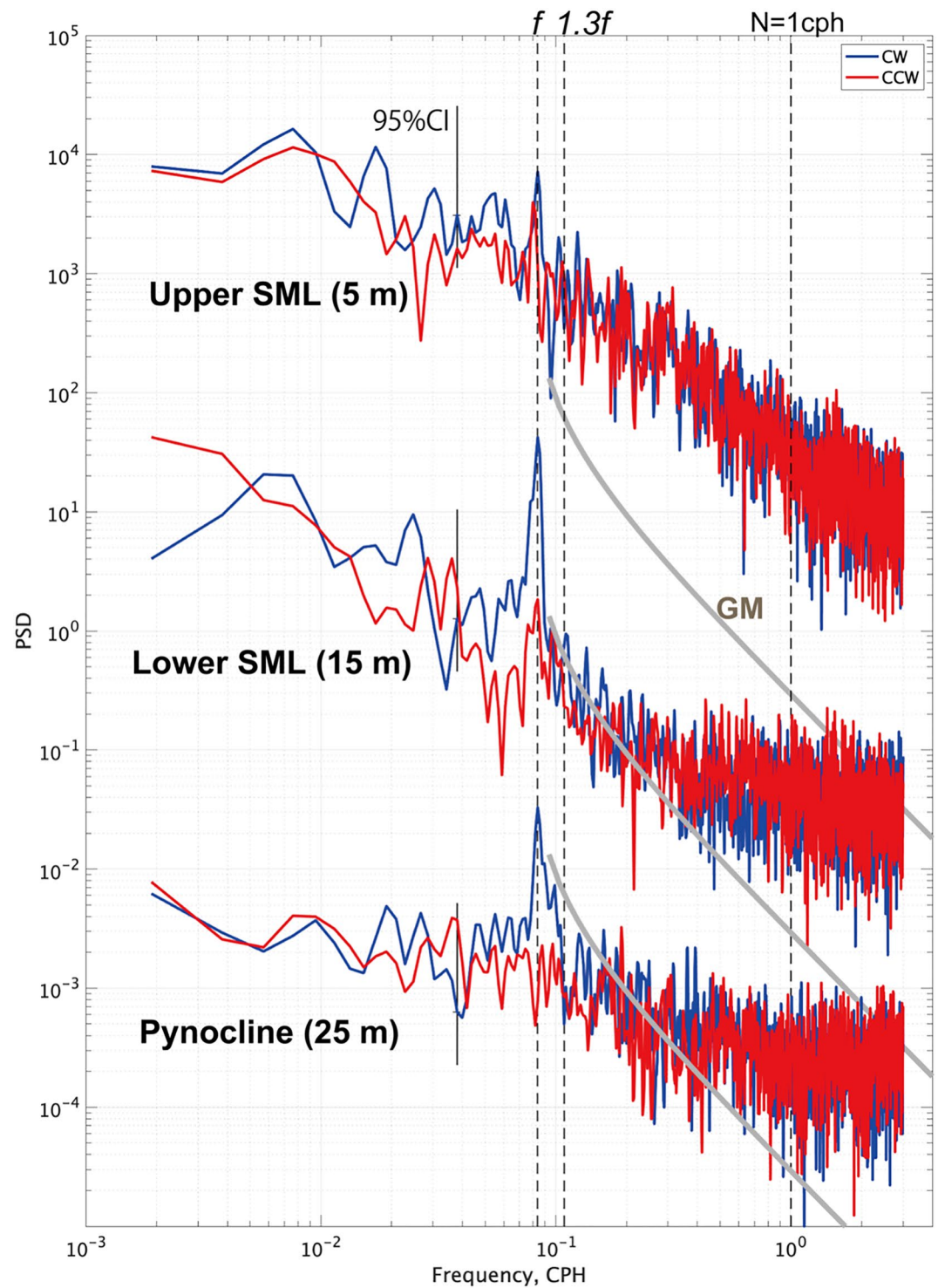


**Figure 12.** Rotary frequency spectrum of the ice–ocean boundary layer-adjusted horizontal current at depths of 5 m, 15 and 25 m, representing upper surface mixed layer (SML), lower SML, and pynocline, respectively (yellow lines in Figure 3). Vertical dashed lines show frequencies of  $f$ ,  $1.3f$ , and  $N = 1.0$  cph. Gray thick curves show the canonical spectrum by Garrett and Munk (1975). Vertical bars in black show the 95% confidence interval. For the convenience, the spectral curves are displayed with a two-order offset in magnitude with each other.

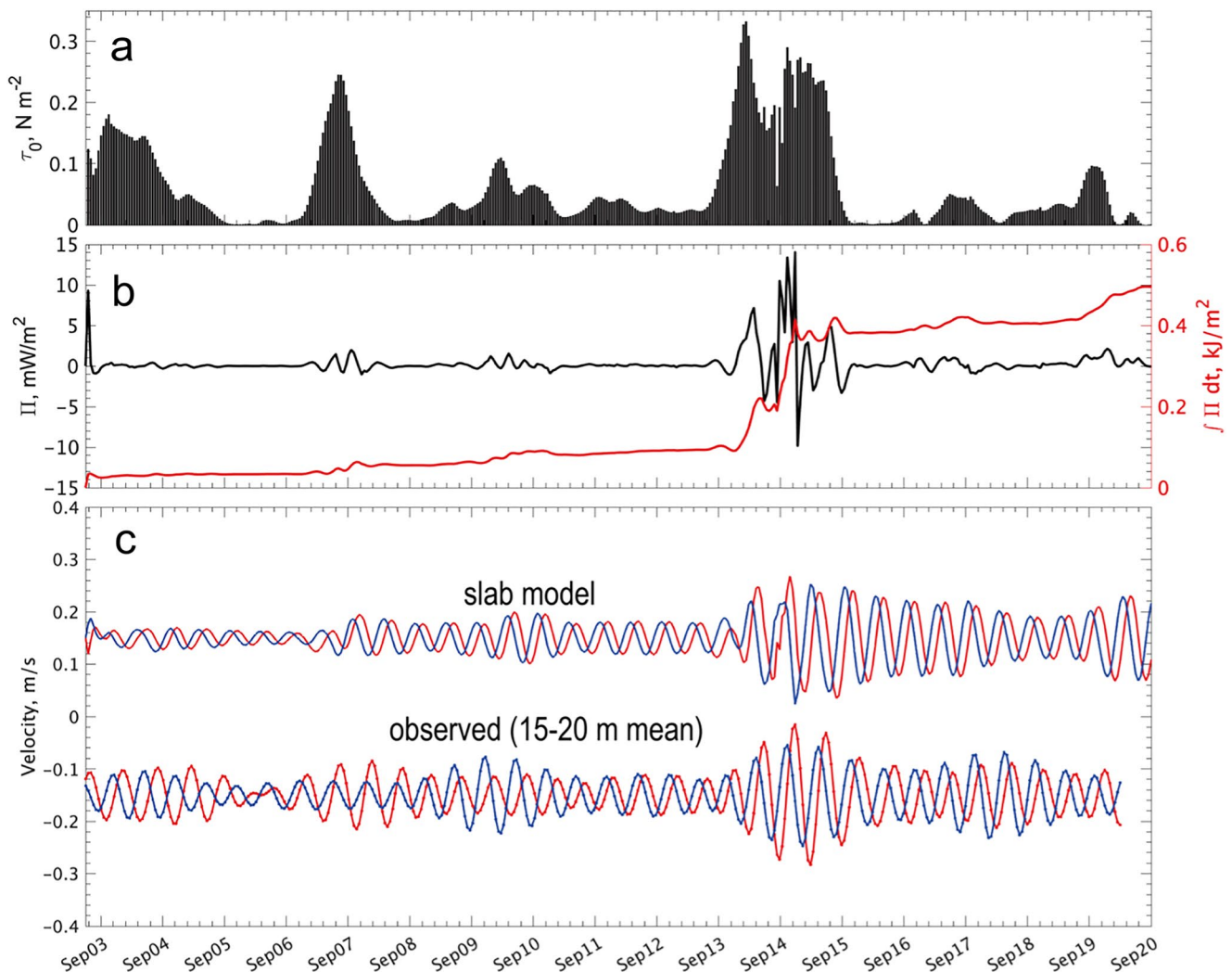


**Figure 13.** Results of surface mixed layer (SML) slab calculation: (a) ice-to-ocean interfacial stress,  $\tau_0$ , (b) kinetic energy flux in black and accumulated energy input in red, and (c) predicted inertial current in SML, where red and blue respectively show zonal and meridional components. In (c), an observed current (ice–ocean boundary layer adjusted) is also shown, which is vertically averaged for 15–20 m in depth and is band-passed for 0.9–1.1f in frequency.

## 5. Turbulence in the Ice-Ocean Boundary Layer (IOBL)

### 5.1. Mixing Layer Versus Mixed Layer

Here, we consider the concept of a “mixing layer,” whose depth is expressed by  $D_{\text{MIL}}$  (e.g., Lombardo & Gregg, 1989) (Figures 9c–9e). In our study,  $D_{\text{MIL}}$  is determined as the depth where  $\epsilon$  first drops below  $3.0 \times 10^{-8} \text{ W kg}^{-1}$ , which is about 40 times larger than the noise level of the MSS instrument (cf., Fer & Sundfjord, 2007). In general, the mixing layer represents where strong mixing is actively present, while “mixed layer” is more widely used to indicate the region that was subject to mixing processes resulted from surface boundary conditions in the recent past.

In a scatter plot of  $D_{\text{MIL}}$  versus  $D_{\text{ML}}$  (Figure 14a), there are two distinct groups:  $D_{\text{MIL}}/D_{\text{ML}} \geq 1$  and  $D_{\text{MIL}}/D_{\text{ML}} \leq 1$ . This distribution highly depends on the magnitude of  $\epsilon$ . For the group of  $D_{\text{MIL}}/D_{\text{ML}} > 1$ ,  $D_{\text{MIL}}$  is comparatively large, whose average is 24.4 m with a standard deviation of 3.0 m, containing a larger median  $\epsilon$  for this group is 4.2 with an IQR of  $6.5 \times 10^{-7} \text{ W kg}^{-1}$ . The result of  $D_{\text{MIL}} > D_{\text{ML}}$  under significant mixing is consistent with earlier reports from the marginal ice zone (MIZ) close to Svalbard (e.g., Fer & Sundfjord, 2007). In contrast, for the group of  $D_{\text{MIL}}/D_{\text{ML}} \leq 1$ , the mixing layer is underdeveloped, and the mean dissipation is low. The average of  $D_{\text{MIL}}$  is 9.3 m with a standard deviation of 3.3 m, while the median value of  $\epsilon$  is  $0.3 \times 10^{-7} \text{ W kg}^{-1}$  with an IQR of  $0.3 \times 10^{-7} \text{ W kg}^{-1}$  (Figure 14a).

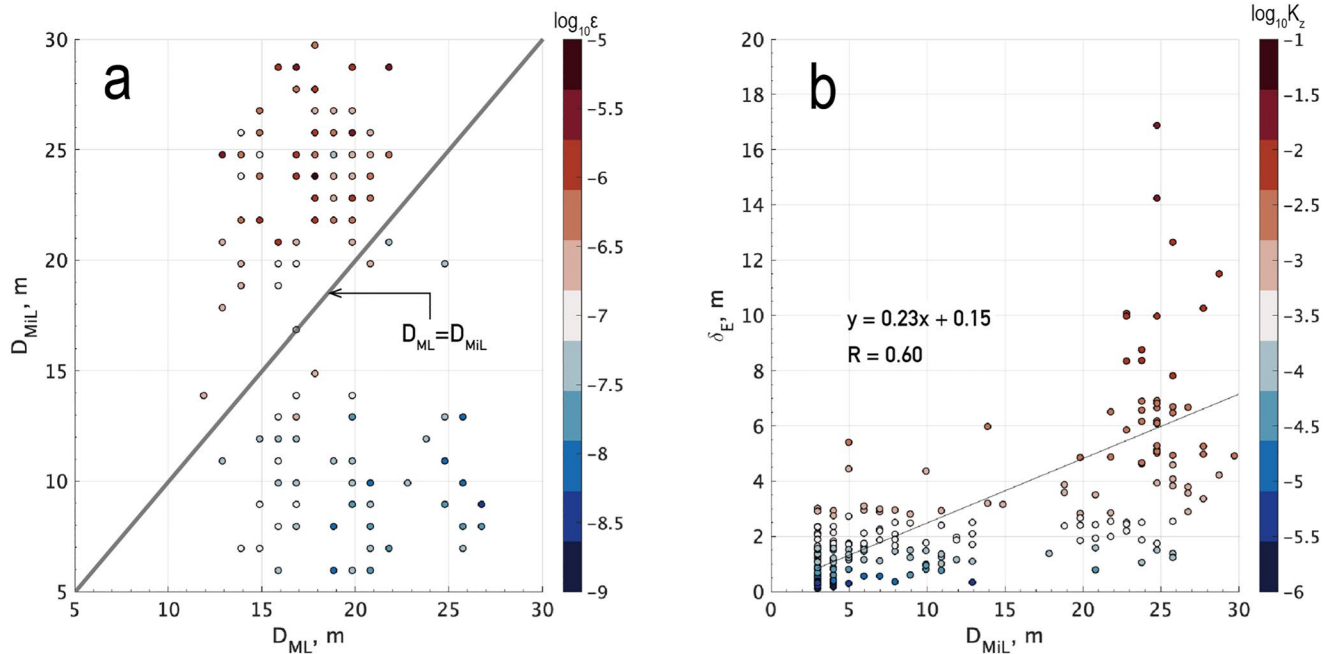


**Figure 14.** Scatter diagrams: (a)  $D_{ML}$  versus  $D_{MIL}$ , and (b)  $D_{MIL}$  versus the Ekman depth,  $\delta_E$ . In (a) and (b), color of dots show magnitudes of  $\log_{10}(\epsilon)$  and  $\log_{10}(K_z)$ , respectively. In (a), the solid line shows the line of  $D_{ML}/D_{MIL} = 1$ , while in (b) the solid line shows the regression with the formulae and the value of the correlation coefficient,  $R$ .

## 5.2. Vertical Profiles of Turbulence Variables

From the repeated MSS measurements, a series of turbulence-related variables were calculated for depths close to those of the SML (Figures 8e–8k). The TKE dissipation rate,  $\epsilon$ , is high within the weakly stratified SML and rapidly drops down to the depth of the  $N$  maximum around 20 m (Figure 8e). In the statistics,  $\epsilon$  is estimated as the median of  $6.3 \times 10^{-8} \text{ W kg}^{-1}$  with an IQR of  $34 \times 10^{-8} \text{ W kg}^{-1}$  at a depth of  $0.2 \leq |z|/D_{ML} \leq 0.9$ , while it is  $8.8 \times 10^{-8} \text{ W kg}^{-1}$  with an IQR of  $24 \times 10^{-8} \text{ W kg}^{-1}$  at  $0.9 < |z|/D_{ML} \leq 1.1$  (Table 2). The upper limit imposed for the analysis of the SML interior, that is,  $|z|/D_{ML} = 0.2$ , is due to the reduced MSS data quality within top 3 m, where the instrument's descending speed is low (see Section 2.2).

According to the MSS observations, our estimate of  $K_z$  shows a substantial variation within the SML, ranging between orders of  $10^{-5}$ – $10^{-3} \text{ m}^2 \text{ s}^{-1}$  (Figure 8f). Correspondingly,  $K_z$  yields estimates of the vertical buoyancy flux  $\langle w'b' \rangle$  and the vertical heat flux  $\langle w'T' \rangle$  as a function of depth (Figures 8g and 8h). Turbulent fluxes in terms of the vertical buoyancy and heat fluxes are directed upwards within the SML depths. A positive  $\langle w'b' \rangle$  is interpreted as an increase of the rate of potential energy, resulting from entrainment that is aided by turbulence within the pycnocline (Thorpe, 2005). The upward heat flux is attributable to the underlying relatively warm waters residing at 20–30 m depth (Figure 8a). The magnitudes of  $\langle w'b' \rangle$  show a median of  $1.5 \times 10^{-8} \text{ m}^2 \text{ s}^{-3}$  (IQR:  $9.5 \times 10^{-8} \text{ m}^2 \text{ s}^{-3}$ ) within the SML at  $0.2 \leq |z|/D_{ML} \leq 0.9$ , while a median of  $1.8 \times 10^{-8} \text{ m}^2 \text{ s}^{-3}$  (IQR:  $5.3 \times 10^{-8} \text{ m}^2 \text{ s}^{-3}$ ) near the pycnocline at  $0.9 < |z|/D_{ML} \leq 1.1$  (Table 2). The median magnitudes of turbulent heat flux,  $\rho C_p \langle w'T' \rangle$ , are  $0.62 \text{ W m}^{-2}$  and  $0.34 \text{ W m}^{-2}$  inside SML and near the pycnocline, respectively.

The turbulence transports the momentum flux  $\langle u'w' \rangle$  downward (negative values) from the surface level (Figure 8k). It is estimated as a median of  $-7 \times 10^{-6} \text{ m}^2 \text{ s}^{-2}$  with an IQR of  $34 \times 10^{-6} \text{ m}^2 \text{ s}^{-2}$  and a median of  $-12 \times 10^{-6} \text{ m}^2 \text{ s}^{-2}$  with an IQR of  $31 \times 10^{-6} \text{ m}^2 \text{ s}^{-2}$  within the SML and near the pycnocline, respectively. The turbulent viscosity  $A_z$  is derived by a division of  $\epsilon$  by a squared shear of horizontal velocity (Figures 8i and 8j; see also Section 2.3). Consequently, at the depths of the strongest current shear, namely within the top 10 m,  $A_z$  is significantly reduced to an order of  $10^{-4} \text{ m}^2 \text{ s}^{-1}$ . This is evident from the intensified shear near the surface (Figure 8i). In the meantime,  $A_z$  shows a local peaks of an order of  $10^{-3} \text{ m}^2 \text{ s}^{-1}$  at depths between 10 and 25 m, corresponding to the local shear maximum, where  $\epsilon$  remain large enough as a response to the critical shear (which is argued in the following subsections) (Figures 8e, 8i and 8j).

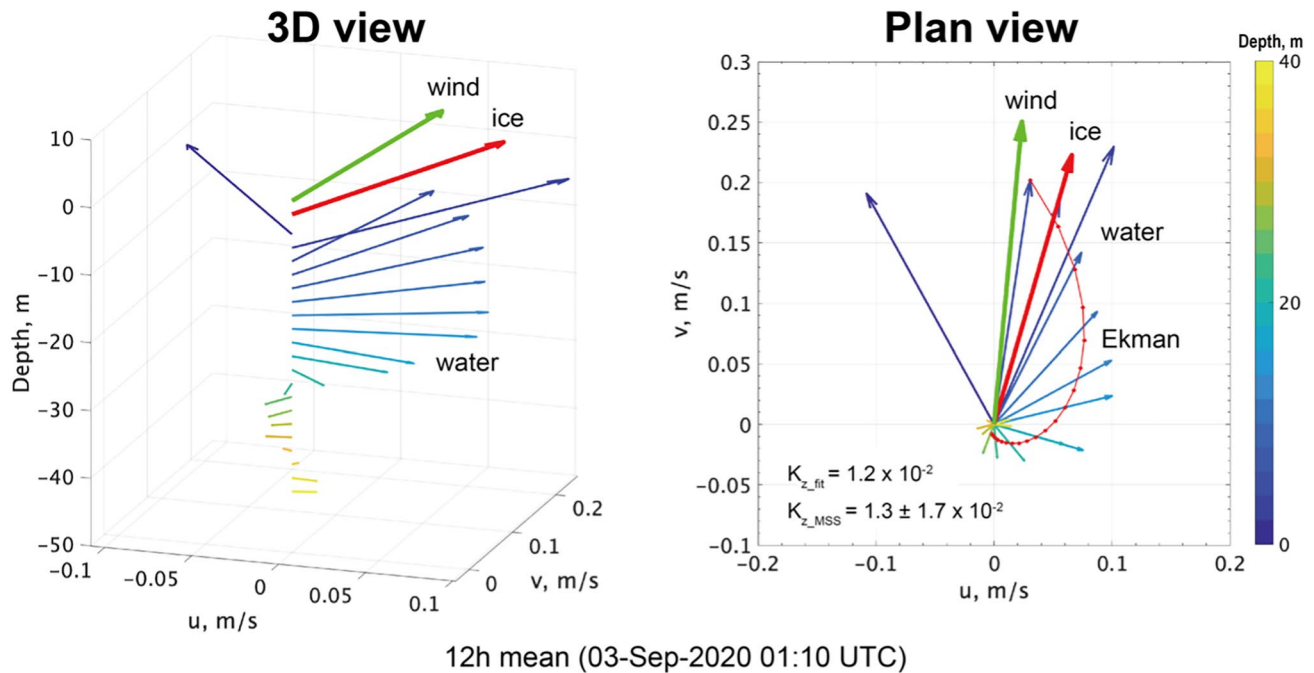


**Figure 15.** The Ekman spiral observed on 3 September 2020: horizontal vectors of wind (green) at 2-m height, ice drift (red), and IOBL-adjusted water currents (blue to yellow) from 5 to 40 m depth. Velocities are the 12-hr averages. Left and right panels respectively show three- and two-dimensional representations. The dot-solid red curve shows the best-fit solution of logarithmic boundary layer theory, where  $K_{z\_fit} = 1.2 \times 10^{-2} \text{ m}^2 \text{ s}^{-1}$ . The  $\epsilon$ -based estimate gives the value of  $K_{z\_MSS} = 1.3 \pm 1.7 \times 10^{-2} \text{ m}^2 \text{ s}^{-1}$ .

### 5.3. The Ekman Layer

The Ekman current in the upper ocean, resulting from the surface Reynolds stress, is known to rotate CW with increasing depth in the Northern Hemisphere as a joint effect of the earth's rotation and friction forces (e.g., Hunkins, 1966; Leppäranta & Omsted, 1990; Shirasawa & Ingram, 1997). The depth-dependent current structure is the so-called Ekman spiral (Figure 15). The Ekman currents can be modeled by the simplified analytic solution given by Pedlosky (1987):  $u(z) = U_0 \left(1 - e^{\frac{z}{\delta_E}} \cos(z/\delta_E)\right)$  and  $v(z) = U_0 e^{\frac{z}{\delta_E}} \sin(z/\delta_E)$ , where  $U_0$  represents the surface current. The thickness of the Ekman layer,  $\delta_E$ , is typically expressed by  $\delta_E = \sqrt{\frac{2K_z}{f}}$ , with the turbulent diffusivity  $K_z$ .

We took a 12-hr average for the ADCP horizontal velocities during 1:10–13:10 UTC on 3 September, revealing a distinct Ekman spiral (Figure 15). For comparison, the least-square best-fit curve from the Ekman theory is overlain with the observed current, where we obtained  $K_{z\_fit} = 1.2 \times 10^{-2} \text{ m}^2 \text{ s}^{-1}$  and evaluated  $\delta_{E\_fit} = 12.8 \text{ m}$ . We assume that  $U_0$  coincides with the current observed at 5 m depth. During the same time, the MSS-based diffusivity from six consecutive profiles yields the median of  $K_{z\_MSS} = 1.3 \times 10^{-2} \text{ m}^2 \text{ s}^{-1}$  with an IQR of  $1.7 \times 10^{-2} \text{ m}^2 \text{ s}^{-1}$  as an average over the SML depth ( $|z| \leq D_{ML}$ ), which is also consistent with the best-fit value from the ADCP current. This estimate of  $\delta_E$  is applied to all 250 MSS profiles (Figure 14b). The calculated  $\delta_E$  varies in a range of 0–20 m, with the mean of 2.7 m (Table 3; Figure 14b). We found only six out of the 250 profiles in which  $\delta_E$  exceeds 10 m, equivalent to  $K_z \geq 0.8 \times 10^{-2} \text{ m}^2 \text{ s}^{-1}$ . In comparison with the mixing layer depth,  $D_{MIL}$ , we find a positive correlation ( $R = 0.51$ ) between them (Figure 14b), which suggests a relation of  $\delta_E \approx 0.2D_{MIL}$  particularly when  $K_z = O(<10^{-3} \text{ m}^2 \text{ s}^{-1})$ .

### 5.4. Responses to a Storm

During and after the second storm, an intensive sampling period was initiated on 14–15 September, resulting in a series of 86 consecutive MSS casts (Table 1, Figure 16). This data set enables us to conduct a detailed investigation of the temporal and vertical development of entrainment and deepening of the SML. According

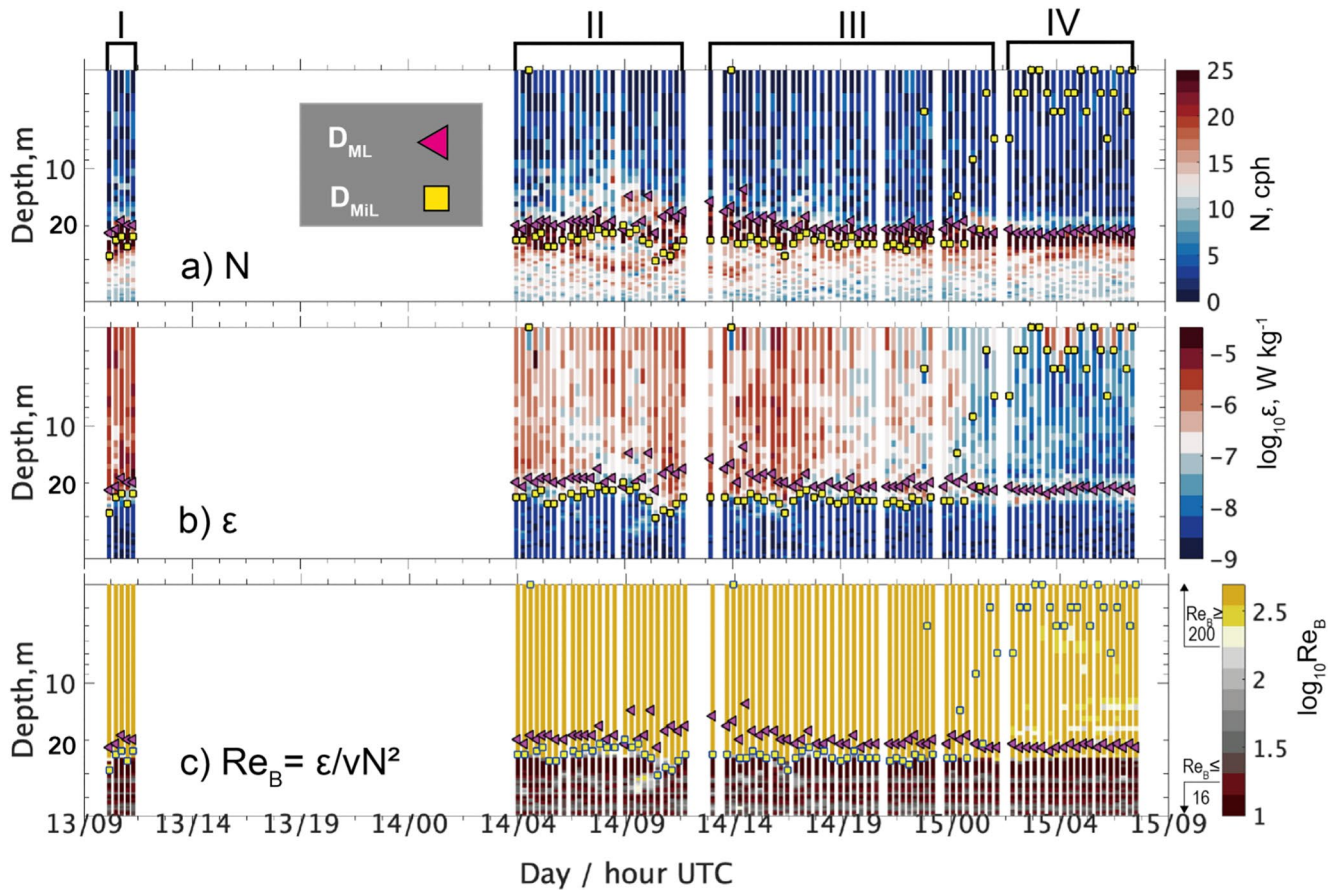


**Figure 16.** Time-vertical section of (a)  $N$ , (b)  $\log_{10}(\epsilon)$ , and (c) turbulent Reynolds number  $Re_B = \frac{\epsilon}{\nu N^2}$  during the storm event in the mid-September (see also Figure 9). Yellow squares and magenta triangles show the depths of the mixed layer ( $D_{ML}$ ) and the mixing layer ( $D_{MiL}$ ), respectively. In (c),  $Re_B \geq 200$  (shaded in yellow) and  $Re_B \leq 16$  (shaded in dark red) indicate thresholds of the isotropy and of significant turbulence, respectively (Gregg & Sanford, 1988).

to the sequential measurements, the spatiotemporal evolution of  $\epsilon$  could be explained by that of  $u_0^*$  (Table 1). Particularly, when  $u_0^* > 1.0 \text{ cm s}^{-1}$  (i.e., Term I to III), the vertical extension of  $\epsilon > O(10^{-6}) \text{ W kg}^{-1}$  built up further beyond the depth of mixed layer, as shown by  $D_{MiL} > D_{ML}$ . When the surface stress decreased below the level of  $u_0^* = 1.0 \text{ cm s}^{-1}$  (Term IV),  $\epsilon$  was largely attenuated in both time and vertical extent (i.e., red shading to blue shading), so that the mixing region, where  $\epsilon > 3 \times 10^{-8} \text{ W kg}^{-1}$ , immediately shoaled toward the surface (Figure 16b).

The evolution of  $N(t, z)$  shows that during 6 and 10 a.m. UTC on 14 September, the region of high stratification near the SML base was partly destroyed by the diapycnal mixing, and consequently the pycnocline was markedly dispersed (Figure 16a). Interestingly,  $\epsilon$  near or slightly above the pycnocline was reduced by roughly an order of magnitude (Figure 16b). Furthermore, between 9 and 10 a.m., the mixing layer abruptly deepened to exceed 30 m (yellow squares in Figure 16).

To assess the intensity of the turbulent mixing, we calculated the turbulent Reynolds number as  $Re_B = \frac{\epsilon}{\nu N^2}$  (Gregg & Sanford, 1988) (Figure 16c). Generally, this number implies a state of fully developed turbulence in the isotropic condition when  $Re_B \geq 200$ , while a state of a non-significant turbulence and negligible diapycnal buoyancy flux will be met when  $Re \leq 16$ . Our results show that the entire mixing layer (bounded by  $|z| = D_{MiL}$ ), and the depth below it, reach  $Re_B \geq 200$  and  $Re_B \leq 16$ , respectively. Fully developed turbulence indicated by  $Re_B \geq 200$  can be found at depths of  $D_{ML} \leq |z| \leq D_{MiL}$ , which continued even after the surface momentum input had been reduced. This persisting turbulence in the SML can be attributed to the NIW shear as a consequence of the resonant inertial motion between ice and water (Figures 11c and 13).

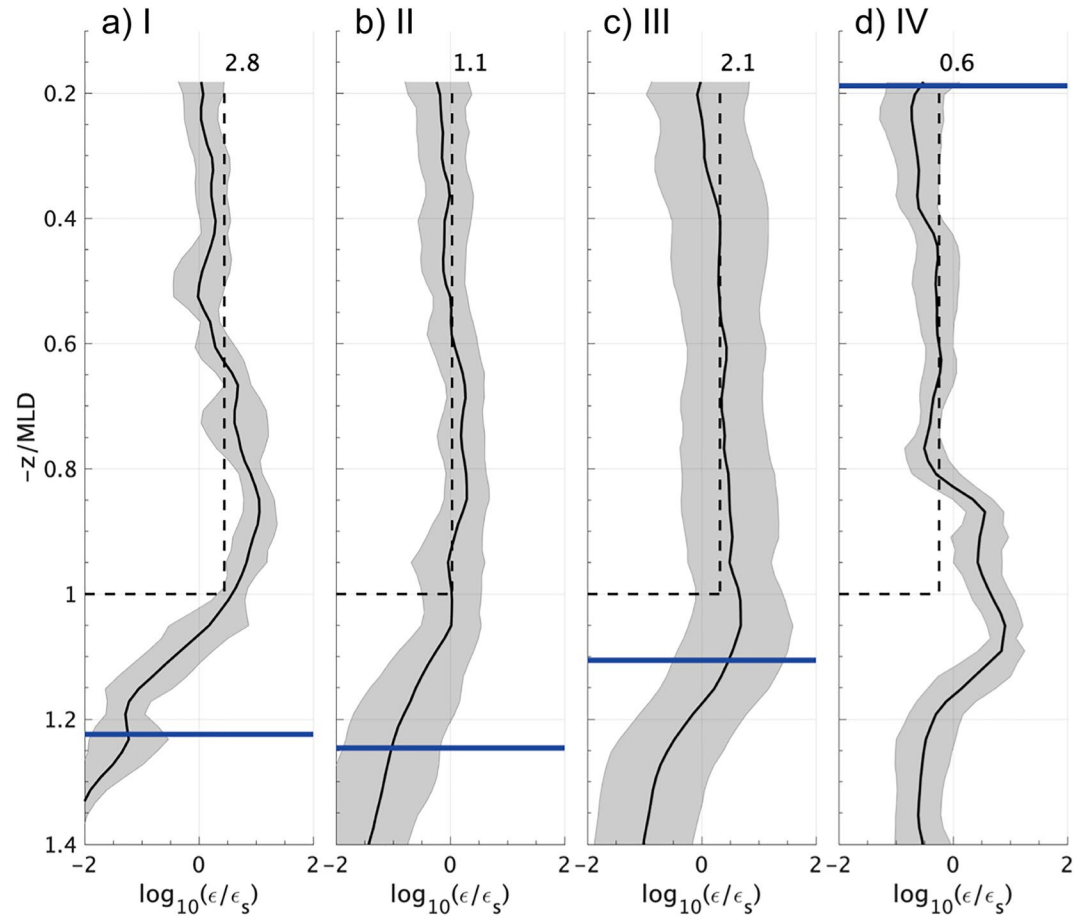


**Figure 17.** Vertical profiles of  $\epsilon$  normalized by  $\epsilon_s(z) = (u_0^*)^3 / \kappa |z|$  (a–d) Terms I, II, III, and IV. Bold curves and gray envelopes show the MLE and the 95% confidence interval, respectively. The horizontal blue lines represent the mean depths of the mixing layer ( $|z| = D_{\text{ML}}$ ). Digits indicate the median values of  $\frac{\epsilon}{\epsilon_s}$  for a range of  $0.2 < \frac{|z|}{D_{\text{ML}}} < 1.0$ .

We next investigate the vertical profiles of observed dissipation rate for the storm event around 13–15 September (Figure 17). Note that in this analysis the vertical coordinate,  $z$ , is scaled by  $D_{\text{ML}}$ . The observed profiles of  $\epsilon$  are normalized by a mechanical portion of the *LoW* variation (e.g., Fer & Sundfjord, 2007; Lombardo & Gregg, 1989; Lozovatsky et al., 2005):

$$\epsilon_s(z) = (u_0^*)^3 / \kappa |z| \quad (9)$$

where  $\kappa = 0.4$  again. According to the analysis, the fluxes at the ice-ocean interface are  $u_0^* = 1.1 \text{ cm s}^{-1}$  as a median value with an IQR of  $1.0 \text{ cm s}^{-1}$  and  $\langle w'b' \rangle_0 = -3.2 \times 10^{-9} \text{ m}^2 \text{ s}^{-3}$  as a median with an IQR of  $4.1 \times 10^{-9} \text{ m}^2 \text{ s}^{-3}$ . For the entire storm period, a best-fit for  $\epsilon(z)$  yields  $1.68 \epsilon_s$ . As argued already in Section 2.1, the choice of  $z_0$ , either 0.007 or 0.01 m, could affect the result of  $\epsilon_s$  via  $u_0^*$ , by roughly 16% at maximum. Therefore, it would be safe to say that the feasible range of the estimate is  $\epsilon/\epsilon_s = 1.4\text{--}1.7$ . The estimate above is supported by earlier works by Lombardo and Gregg (1989), who proposed a best-fit regression of  $\epsilon = 1.76(u_0^*)^3 / \kappa |z|$  in the open water of the California Current. Fer and Sundfjord (2007) also suggested  $\epsilon/\epsilon_s = 4\text{--}4.5$  in the MIZ near Svalbard.

We also examined another scaling of  $\epsilon$  by incorporating the surface buoyancy flux (Lozovatsky et al., 2005):

$$\epsilon_s(z) = (u_0^*)^3 / \kappa |z| + c_m J_B \quad (10)$$

where  $J_B = -\langle w'b' \rangle$  and  $c_m$  is an empirical constant. As already shown, the surface buoyancy flux tends to be unstable (i.e.,  $\langle w'b' \rangle < 0$ ) during early September, which may help the entrainment increase by producing overturning near the surface. For the mid- and post-storm periods, the optimal choice of  $c_m$  is 14.5, with  $\langle \epsilon/\epsilon_s \rangle = 0.99$

for the range of  $|z| = 0.3\text{--}1.0 D_{ML}$ . The coefficient  $c_m = 14.5$  is too large compared to the findings in related studies (cf.  $c_m = 3.7$  and  $J_B = 3 \times 10^{-8} \text{ m}^2 \text{ s}^{-3}$  reported by Lozovatsky et al., 2005). In our case, the buoyancy term was one order of magnitude smaller than  $(u_0^*)^3 / \kappa |z|$ , thus a larger  $c_m$  is needed to compensate.

Further, we divide the storm period into four shorter segments (Term I–IV; see also Table 1) and the best-fit coefficients vary in a range of 0.6–2.8 (Figure 17). Vertical profiles of  $\log_{10}(\epsilon/\epsilon_s)$  are nearly vertical at  $0.2 < |z|/D_{ML} < 1.0$ . During the earlier periods of the storm passage (Term I–III), the mixing layer depth,  $D_{ML}$ , was 20%–30% deeper than  $D_{ML}$  (red box in Figures 9c–9e). During Term IV, the observed  $\epsilon$  is scaled to be rather small:  $\epsilon/\epsilon_s = 0.67$ , as the winds had diminished (Figure 17d). In this Term, there is a distinctive peak near the base of the SML at  $|z| = 0.9\text{--}1.2 D_{ML}$ , where  $\epsilon/\epsilon_s$  was nearly one order of magnitude greater than the remaining part. This enhanced turbulence is explained by the localized NIW activity around the pycnocline (Figure 11).

### 5.5. Bulk Estimates of Energy Balance

To evaluate the transport of the air-to-ocean turbulent energy, we calculate the bulk estimates of the energy fluxes in the atmospheric and oceanic boundary layers (Figure 9a), respectively given by  $E_{10} = \tau_a U_{10}$  and  $E_0 = \rho_w (u_0^*)^3$  (Richman & Garrett, 1977). In this study,  $U_{10}$  is the wind speed at 10 m height and the air stress  $\tau_a = \rho_a C_a U_{10}^2$ , with the air density  $\rho_a = 1.25 \text{ kg m}^{-3}$  and the air drag coefficient  $C_a = 1.3 \times 10^{-3}$  (Fisher & Lytle, 1998). Following the convention in the related studies (e.g., Fer & Sundfjord, 2007),  $\tau_a$ ,  $U_{10}$ , and  $u_0^*$  represent vector magnitudes, that is, the direction is omitted. In Figure 9a, an SML-integrated TKE dissipation rate,  $\epsilon_I = \int_{D_{ML}}^{0.2 D_{ML}} \rho_w \epsilon dz$ , is also shown (Oakey & Elliot, 1982). For depths  $< 3 \text{ m}$  measurements of  $\epsilon$  are unreliable, so it is interpolated with the *LoW* approximation of Equation 9.

The temporal variations of  $E_{10}$ ,  $\epsilon_I$  and  $E_0$  are highly correlated (Figure 9a). The correlation coefficients between  $E_{10}$  and  $\epsilon_I$ , and  $E_0$  and  $\epsilon_I$  are  $R = 0.68$  and  $R = 0.87$ , respectively (Figure 18). Our calculations yield approximate relations of  $\epsilon_I \approx 0.012 E_{10}$  and  $\epsilon_I \approx 11 E_0$ . This result is roughly consistent with related studies: for example,  $\epsilon_I \approx 0.01 E_{10}$  and  $\epsilon_I = \sqrt{\frac{\rho_a}{\rho_w}} C_D \approx 8 E_0$ , where  $C_D = 1.3 \times 10^{-3}$  is the air-ocean drag coefficient, off Nova Scotia (Oakey & Elliot, 1982; blue lines in Figure 18). Lozovatsky et al. (2005) and Richman and Garrett (1977) suggested a larger rate of energy consumption of the wind work in the near-surface water:  $\frac{\epsilon_I}{E_{10}} = 0.03\text{--}0.07$  and  $\frac{\epsilon_I}{E_0} = 0.02\text{--}0.1$ , respectively.

We next examine the TKE balance within the IOBL (Figure 19). For the IOBL physics, the TKE production due to the vertical shear of oceanic currents that result from the ice drift is expressed by  $P_{sh} = \frac{u^{*3}}{\lambda_{LTC}}$ , where  $\lambda_{LTC}$  is the mixing length scale based on the LTC (i.e., Equation 4) and  $u^* = u^*(z)$  is the friction velocity at an arbitrary depth. For the determination of  $\lambda_{LTC}$ , we adopt the following expression:

$$\lambda_{LTC}(z) = \begin{cases} \lambda_{LoW} = \kappa |z|, & |z| < z_{LoW} \\ \lambda_{max} = \Lambda_* u_0^* \eta^2 / |f|, & |z| \geq z_{LoW} \end{cases} \quad (11)$$

where  $z_{LoW} = \Lambda_* u_0^* \eta^2 / (\kappa |f|)$  and  $\Lambda_* = 0.028$  is the universal similarity parameter. According to the *LoW* concept, we assume that  $\lambda_{LTC}$  linearly grows with distance from the ice-ocean interface until it reaches the maximum length,  $\lambda_{max}$ . The stability factor is given by  $\eta = \left[ 1 + \frac{\Lambda_* u_0^*}{\kappa |f| R_c L_O} \right]^{-1/2}$ , which has a typical range of 0.9–1.1.  $R_c$  is the critical flux Richardson number, and assumed as 0.2. The local friction speed  $u^*(z)$  as a function of  $z$  is parameterized by the analytic solution of the Ekman stress equation:  $u^*(z) = u_0^* \exp[z/\delta_E]$  and  $\delta_E = \sqrt{\frac{2K_{z_{max}}}{f}}$ , where  $K_{z_{max}} = u_0^* \lambda_{max}$  (McPhee & Martinson, 1994).  $K_{z_{max}}$  is independently obtained from the estimate of MSS-based  $K_z$  that uses the invariant approximation of  $\Gamma = 0.2$  (Figure 8f). Nonetheless, they show a positive correlation of 0.57, similar to the value reported by Fer and Sundfjord (2007).

We focus on the periods of enhanced turbulent mixing during the mid-storm (Term II) and the post-storm (Term IV) segments (Table 1; Figure 19). During Term II, the mixing length  $\lambda_{LTC}$  is generally guided by the *LoW* variation down to  $|z| = 0.3\text{--}0.4 D_{ML}$ , below which the mixing length reaches  $\lambda_{max} = 2.2 \text{ m}$  (Figure 19a). On the other hand, Term IV shows a relatively narrower range of  $\lambda_{LoW}$  and is  $< 0.2 D_{ML}$ , with a far smaller  $\lambda_{max}$  of 0.85 m.

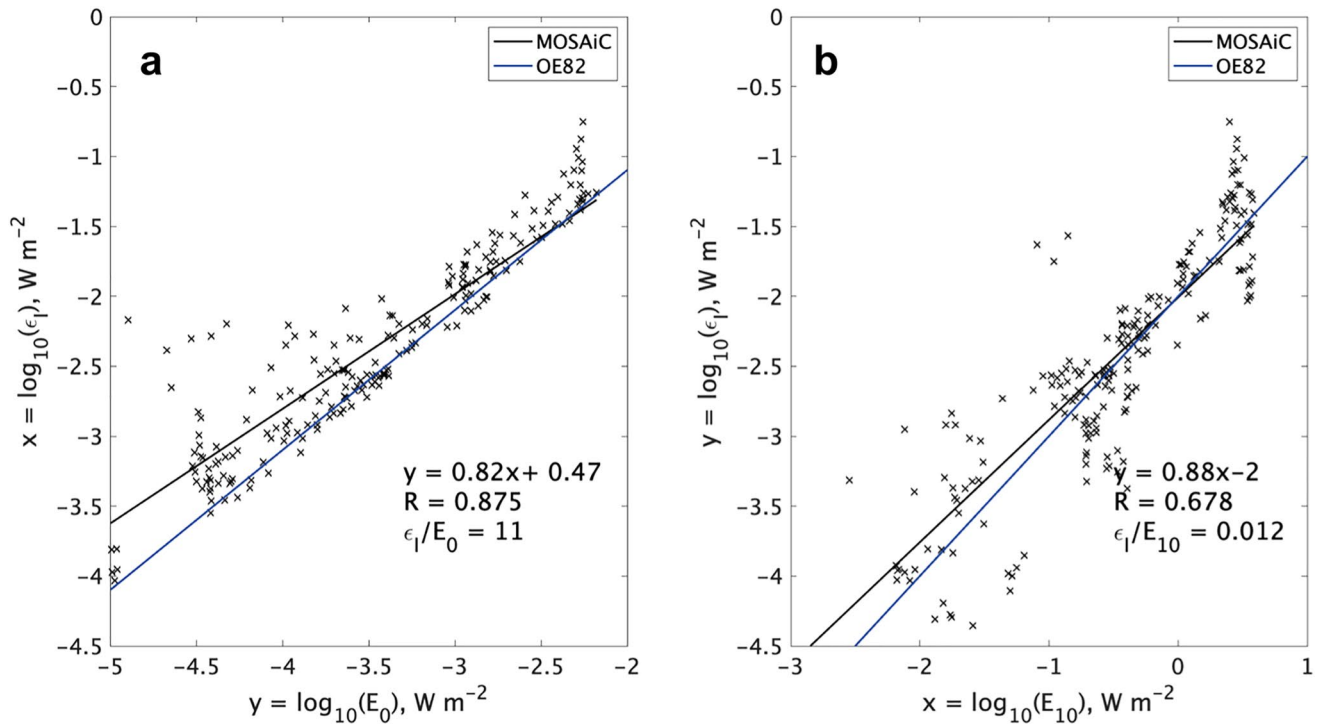


**Figure 18.** Scatter plots: (a) surface mixed layer (SML)-integrated dissipation rate  $\epsilon_I$  versus under-ice energy flux rate,  $E_0$ ; (b)  $\epsilon_I$  versus wind work at 10 m height,  $E_{10}$ . Blue lines are the regressions from the observations in open water (Oakey & Elliot, 1982), while black lines are those from this study.

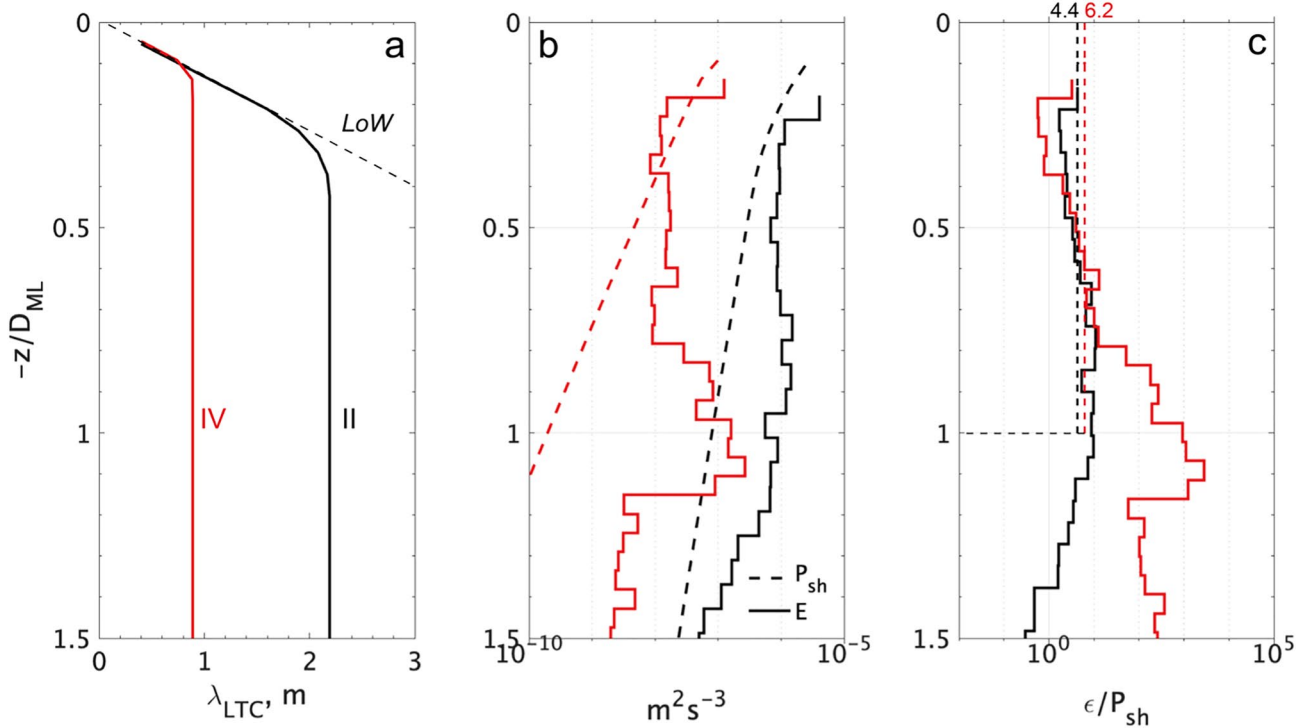


**Figure 19.** Vertical profiles of (a) mixing length,  $\lambda_{LTC}$ , (b) shear-induced turbulent kinetic energy (TKE) production  $P_{sh}$  (dashed) and TKE dissipation rate  $\epsilon$  (bold), and (c) the ratio of  $\epsilon/P_{sh}$ . In each panel, curves in black and red show those for terms II and IV, respectively. In (a), the dashed line shows the mixing length of the Law of the Wall, that is,  $\lambda_{LoW} = \kappa|z|$ . In (b) and (c), the profiles represent the maximum likelihood estimate (MLE) at interpolated 1-m bins. In (a), curves show the averages of all profiles. In (c), dashed vertical lines and number at the top represent median values of  $\epsilon/P_{sh}$  for  $0.2 \leq |z|/D_{ML} \leq 1$ .

Consequently, the prediction curves of  $P_{sh}$  based on the LTC theory result in a sharp difference between the two cases (Figure 19b). Term II begins with a comparatively high value of  $P_{sh}$  to be an order of  $10^{-6} \text{ m}^2 \text{ s}^{-3}$  at the top  $\sim 0.1D_{ML}$ , and then it decreases logarithmically with depth by nearly one order of magnitude at the base of the SML, that is,  $|z|/D_{ML} = 1$ . For Term IV,  $P_{sh}$  begins with a value on an order of  $10^{-8} \text{ m}^2 \text{ s}^{-3}$ , and then quickly drops down to  $\sim 10^{-10} \text{ m}^2 \text{ s}^{-3}$  below  $|z|/D_{ML} = 1$ .

Overall, in the range of  $0.2 \leq |z|/D_{ML} \leq 1$ , the average values of  $\epsilon_{MLE}/P_{sh}$  are 4.4 and 6.2 for Term II and IV, respectively. Here,  $\epsilon_{MLE}$  represents the maximum likelihood estimate (MLE) of  $\epsilon$  from all profiles during each term. For both terms, the observed curve of  $\epsilon_{MLE}$  appears to follow that of  $P_{sh}$  in the logarithmic decay with depth at  $|z| \leq 0.3\text{--}0.4D_{ML}$  (Figures 19b and 19c). The ratio  $\epsilon_{MLE}/P_{sh}$  is closest to unity at  $0.2 \leq |z|/D_{ML} \leq 0.4$  (Figure 19c), but it tends to separate from  $\epsilon_{MLE}/P_{sh} = 1$  at depths of  $|z| \geq 0.5D_{ML}$ . The localized enhancement of  $\epsilon_{MLE}$  at the lower part of the SML is more apparent in the case of Term IV. Here,  $\epsilon_{MLE}$  and  $\epsilon_{MLE}/P_{sh}$  exhibit peaks at  $|z| = 0.8\text{--}1.2D_{ML}$ , reaching orders of  $10^{-7} \text{ m}^2 \text{ s}^{-3}$  and  $10^3$ , respectively. Such enhancement appears to originate from the depth right underneath the point of  $N = 7$  cph (dashed in Figure 11), where  $|z|/D_{ML} = 0.6$  and  $0.8$  for Term II and Term IV, respectively (horizontal lines in Figure 19c).

### 5.6. Shear Instabilities Near the Pycnocline

We suspect that vertical shear of NIW could promote an enhanced  $\epsilon$  near the pycnocline (Figures 17d; 19b). The strong shear along with the concurrent density jump may cause the Kelvin-Helmholtz (K-H) and/or the Holmboe instabilities (e.g., Holmboe, 1962; Strang & Fernando, 2001; Thorpe, 1968). These types of shear instabilities can stir up and entrain the stratified water near the bottom of the SML, resulting in the weakening of the stratification and diffusion of the pycnocline. For the occurrence of the Holmboe instability, a train of billows will develop when the centers of vertical shear of horizontal current and the pycnocline are coincident, but the vertical scale of the current shear is greater than that of the density gradient, typically by a factor of 2–3 (Thorpe, 2005). The Holmboe billows are known to grow more slowly than the K-H billows, but the net amount of mixing is comparable (Smyth & Winters, 2003).

In our case, the pycnocline at the base of the SML is partly overlapped by the vertical shear of NIWs, which may satisfy the necessary conditions of the Holmboe instability (Thorpe, 1968, 2005). According to numerical simulations by Strang and Fernando (2001), the type of instability is inferred from a criterion based on bulk Richardson number,  $Ri_B = \frac{h\Delta b}{(\Delta U)^2}$ , where  $\Delta U$ ,  $\Delta b$ , and  $h$  are the characteristic scales of the current, the buoyancy jump, and the vertical length of shear, respectively. The Holmboe instability exclusively dominates when  $Ri_B > 5.8$ ; the K-H instability dominates when  $Ri_B < 3.2$ ; the mixed regime may occur when  $3.2 < Ri_B < 5.8$ .

For the present situation, we can assume that the scale of vertical shear is related to the vertical wavelength  $\lambda_z$  of the NIW, and therefore  $h \approx \lambda_z = 13$  m (Figure 11). For the typical value of the current speed  $\Delta U$ , we take the amplitude of inertial oscillation within the SML and  $\Delta U = 0.1\text{--}0.15 \text{ m s}^{-1}$  (Figure 13c). The density jump across the pycnocline is  $1.5\text{--}2.0 \text{ kg m}^{-3}$  (Figure 11), equivalent to  $\Delta b = 1.4\text{--}1.9 \times 10^{-2} \text{ m s}^{-2}$ . From the resulting  $Ri_B = 8.3\text{--}11$ , we deduce that a Holmboe instability was occurring during the mid-storm and post-storm periods in mid-September, rather than the K-H instability. Thus, it is inferred that this instability played an important role in transferring the NIW's kinetic energy into the turbulence-scale phenomena near the depth of the SML (Figure 11c), eventually resulting in an erosion of the pycnocline.

## 6. Conclusions

In this study, we examined the ice-ocean boundary layer physics under a consolidated multi-year ice floe in the central Arctic Ocean, with an emphasis on the wind-driven inertial ice drift. The observations were conducted in late August through late September 2020, during the final leg of the MOSAiC expedition (Figure 1a). Along with the tracked ice motions, concurrent profiles of current (Figure 3), hydrography and microstructures (Figure 9) were obtained. Besides this, the ice mass balance observation by an autonomous instrument, SIMBA, was used to investigate temporal and vertical variation of ice interior temperature and the conductive heat flux near the ice-ocean interface (Figure 5).

The LTC calculation showed that at the end of August the basal ice melt transitioned to the refreezing phase (Figure 4). This regime shift can be attributed to drastic changes in the hydrographic properties of the SML,

where the salinity dropped by 2–2.5 psu (Figure 9b). The mixed layer depth was on average  $D_{ML} = 18.4$  m, with a standard deviation of 3 m, and it did not show any significant alternation over the month-long measurement (e.g., Figures 9c and 14a). At the same time, the mixing layer depth was on average  $D_{MIL} = 17.8$  m, with a standard deviation of 8 m, and it showed a larger temporal variation, with a higher dependency on the ice drift speed (Figure 14).

The sea ice drift is highly correlated with the 10-m height wind and the 10-m depth current (IOBL-adjusted) (Figure 6). During the summer months, the inertial motion of sea ice drift was apparently dominant (Figure 7) as a reaction to the atmospheric forcing. According to the slab model prediction (Figure 13) and the rotary spectrum of ADCP current (Figure 12), it is obvious that the inertial ice drift amplified the semi-diurnal motion in the SML. When a pronounced cyclone passed the study area on 13–14 September, the largest amplitude of NIWs were observed near the SML. During this event, the stratification near the SML base was partly eroded by turbulence, resulting in a deepening of the energy-containing region (Figure 16). Following the storm, a packet of NIW accommodated in the stratification at the lower part of the SML (Figure 11). We also found a distinct peak of  $\epsilon$  near the pycnocline at the SML base (Figure 17d). We suspect that the NIW's kinetic energy was effectively translated into turbulent-scale mixing over there through the occurrence of the Holmboe instability (Figure 19).

Based on the microstructure profiler (MSS) measurements for the month-long observation, we found a turbulent energy dissipation rate, diffusivity and viscosity for the SML interior as medians of  $\epsilon = 6 \times 10^{-8}$  W kg<sup>-1</sup> (IQR:  $34 \times 10^{-8}$  W kg<sup>-1</sup>),  $K_z = 32 \times 10^{-5}$  m<sup>2</sup> s<sup>-1</sup> (IQR:  $161 \times 10^{-5}$  m<sup>2</sup> s<sup>-1</sup>), and  $A_z = 10 \times 10^{-4}$  m<sup>2</sup> s<sup>-1</sup> (IQR:  $36 \times 10^{-4}$  m<sup>2</sup> s<sup>-1</sup>), respectively (Table 2; Figure 8). The vertical variation of  $\epsilon$  is scaled to be 1.4–1.7 times of the *Law of the Wall* model,  $\epsilon_s = u_0^{*3}/\kappa|z|$  (Figure 17). From the present observation, the SML-integrated  $\epsilon$  supported good correlations with the cross-boundary energy flux  $E_0$  and the wind work  $E_{10}$ :  $\frac{\epsilon_I}{E_0} \approx 11$  and  $\frac{\epsilon_I}{E_{10}} \approx 0.012$  (Figure 18). These ratios are generally consistent with previous observations in different environments of open water and marginal ice zone.

The ADCP measurements also clearly revealed a spiraling Ekman layer (Figure 15). The turbulent diffusivity predicted from the logarithmic boundary layer theory was comparable to the estimate from the MSS-derived  $K_z$ . The estimate of the Ekman layer depth,  $\delta_E = \sqrt{\frac{2K_z}{f}}$ , applied to the entire observation period, is well correlated with  $D_{MIL}$ , suggesting the relation of  $\delta_E \approx 0.2 D_{MIL}$  (Figure 14b).

From our observations during the MOSAiC expedition, we conclude that knowledge of fresh water distribution in the SML in the Arctic is an essential factor for the accurate estimate of ice-ocean heat exchange, especially for the period of seasonal transition of thermodynamical phase. Increased thermohaline observations in the SML, similar to those presented here, would improve the future prediction of the Arctic climate. With respect to momentum and kinetic energy near the surface, they are temporarily stored as a form of internal waves and then cause local turbulence after a while. Therefore, the balance of mechanical energy around the SML should be considered as the long-term average.

## Data Availability Statement

The data mainly analyzed in this study are retrieved from links below: MSS-derived variables = <https://doi.org/10.1594/PANGAEA.939816>; ADCP velocities = <https://ads.nipr.ac.jp/dataset/A20220221-001>; Positions of drifting buoys = <https://ads.nipr.ac.jp/dataset/A20220221-002>; Meteorological variables = <https://doi.org/10.18739/A2VM42Z5F>; ROV sea ice draft = <https://doi.org/10.1594/PANGAEA.945846>. In this study, all of calculations and drawing procedures were done using MATLAB® version 9.5.0 (R2018b).

## References

- Aagaard, K., Coachman, L. K., & Carmack, E. C. (1981). On the halocline of the Arctic Ocean. *Deep-Sea Research*, 28(6), 529–545. [https://doi.org/10.1016/0198-0149\(81\)90115-1](https://doi.org/10.1016/0198-0149(81)90115-1)
- Carmack, E. C. (2000). In E. L. Lewis (Ed.), *The Arctic Ocean's freshwater budget: Sources, storage and export*. *Freshwater budget of the Arctic Ocean* (pp. 91–126). Kluwer Academic Publishers.
- Cisewski, B., Strass, V. H., Losch, M., & Prandke, H. (2008). Mixed layer analysis of a mesoscale eddy in the Antarctic Polar Front Zone. *Journal of Geophysical Research*, 113(C5), C05017. <https://doi.org/10.1029/2007JC004372>
- Cox, C., Gallagher, M., Shupe, M., Persson, O., & Solomon, A. (2021). *10-meter meteorological flux tower measurements (level 1 raw)*, Multidisciplinary Drifting Observatory for the Study of Arctic Climate (MOSAIC). Central Artic. <https://doi.org/10.18739/A2VM42Z5F>

## Acknowledgments

The work conducted and data used for this study were produced as part of the international Multidisciplinary drifting Observatory for the Study of the Arctic Climate (MOSAIC) with the tag MOSAiC20192020. The authors extend their most sincere gratitude for brave and dedicated efforts during the unprecedented world-wide pandemic to everyone who contributed to successful implementations of the MOSAiC expedition. We also thank Kiyoshi Tanaka of U. Tokyo for the ADCP instrument; Jan Rohde and Julia Regnery of AWI for ROV implementation. We thank all persons involved in the expedition of the Research Vessel Polarstern during MOSAiC in 2019–2020 (AWI\_PS122\_00) as listed in Nixdorf et al. (2021; <http://dx.doi.org/10.5281/zenodo.5179739>). This study was supported by the Japan Society for the Promotion of Science (Grant Nos: JP18H03745; JP18KK0292; JP17KK0083; JP17H04715; JP20H04345; JP22H01296) and by the Grant for Joint Research Program of the Japan Arctic Research Network Center. It is also funded by the Center for Ocean Literacy and Education (COLE) of U. Tokyo for Y. Kawaguchi. This work was also funded by the German Federal Ministry of Education and Research (BMBF) through financing the Polarstern expedition PS122 (N-2014-H-060\_Dethloff); Diatom-ARCTIC (03F0810 A); PEANUTS (03F0804 A). The AWI ROV work was partly funded by the Helmholtz strategic investment Frontiers in Arctic Marine Monitoring (FRAM). The valuable comments from two anonymous reviewers were very helpful to improve the quality of data analyses in the manuscript.

- D'Asaro, E. A. (1985). The energy flux from the wind to near-inertial motions in the surface mixed layer. *Journal of Physical Oceanography*, 15(8), 1043–1059. [https://doi.org/10.1175/1520-0485\(1985\)015](https://doi.org/10.1175/1520-0485(1985)015)
- Fer, I. (2006). Scaling turbulent dissipation in an Arctic fjord. *Deep-Sea Research II*, 53(1–2), 77–95. <https://doi.org/10.1016/j.dsr2.2006/01.003>
- Fer, I., & Sundfjord, A. (2007). Observations of upper ocean boundary layer dynamics in the marginal ice zone. *Journal of Geophysical Research*, 112(C4), C04012. <https://doi.org/10.1029/2005JC003428>
- Fisher, R., & Lytle, V. I. (1998). Atmospheric drag coefficients of Weddell Sea ice computed from roughness profiles. *Journal of Glaciology*, 27, 455–460. <https://doi.org/10.3189/1998aog27-1-455-460>
- Garrett, C. J. R., & Munk, W. H. (1975). Space-time scales of internal waves: A progress report. *Journal of Geophysical Research*, 80(3), 291–297. <https://doi.org/10.1029/JC080i003p00291>
- Gill, A. E. (1982). *Atmosphere-ocean dynamics*. Academic Press.
- Gregg, M. C., & Sanford, T. B. (1988). The dependence of turbulent dissipation on stratification in a diffusively stable thermocline. *Journal of Geophysical Research*, 93(C10), 12381–12392. <https://doi.org/10.1029/jc093ic10p12381>
- Halle, C., & Pinkel, R. (2003). Internal wave variability in the Beaufort Sea during the winter of 1993/1994. *Journal of Geophysical Research*, 108(C7), 310. <https://doi.org/10.1029/2000JC000703>
- Holmboe, J. (1962). On the behavior of symmetric waves in stratified shear layers. *Geophys. Publ.*, 24, 67–113.
- Hunkins, K. (1966). Ekman drift current in the Arctic Ocean. *Deep-Sea Research*, 13(4), 607–620. [https://doi.org/10.1016/0011-7471\(66\)90592-4](https://doi.org/10.1016/0011-7471(66)90592-4)
- Jackson, K., Wilkinson, J., Maksym, T., Meldrum, D., Beckers, J., Haas, C., & Mackenzie, D. (2013). A novel and low-cost ice mass balance buoy. *Journal of Atmospheric and Oceanic Technology*, 30(11), 2676–2688. <https://doi.org/10.1175/JTECH-D-13-00058.1>
- Katlein, C., Anhaus, P., Arndt, S., Krampe, D., Lange, B. A., Matero, I., et al. (2022). Sea-ice draft during the MOSAiC expedition 2019/20. *PANGAEA*. <https://doi.pangaea.de/10.1594/PANGAEA.945846>
- Katlein, C., Mohrholz, V., Sheikin, I., Itkin, P., Divine, D. V., Stroeve, J., et al. (2020). Platelet ice under Arctic pack ice in winter. *Geophysical Research Letters*, 47(16), e2020GL088898. <https://doi.org/10.1029/2020GL088898>
- Kawaguchi, Y., Hutchings, J. K., Kikuchi, T., Morison, J. H., & Krishfield, R. A. (2012). Anomalous sea-ice reduction in the Eurasian basin of the Arctic Ocean during summer of 2010. *Polar Science*, 6(1), 39–53. <https://doi.org/10.1016/j.polar.2011.11.003>
- Kawaguchi, Y., Koenig, Z., & Hoppman, M. (2021a). *ADCP velocity data during leg 5 of MOSAiC expedition with R/V Polarstern, 0.00*. Arctic Data archive System (ADS). <https://doi.org/10.17592/001.2022022101>
- Kawaguchi, Y., Koenig, Z., & Hoppman, M. (2021b). *Geographical positioning data from Argo buoys during MOSAiC expedition, 0.00*. Arctic Data archive System (ADS). <https://doi.org/10.17592/001.2022022102>
- Kawaguchi, Y., Nishino, S., Maeno, K., Takeda, H., Ohshima, K., & Oshima, K. (2016). Enhanced diapycnal mixing due to near-inertial internal waves propagating through an anticyclonic eddy in the ice-free Chukchi Plateau. *Journal of Physical Oceanography*, 46(8), 2457–2481. <https://doi.org/10.1175/JPO-D-15-0150.1>
- Leaman, K. D., & Sanford, T. B. (1975). Vertical energy propagation of inertial waves: A vector spectral analysis of velocity profiles. *Journal of Geophysical Research*, 80(15), 1975–1978. <https://doi.org/10.1029/JC080i015p01975>
- Lei, R., Cheng, B., Heil, P., Vihma, T., Wang, J., Ji, Q., & Zhang, Z. (2018). Seasonal and interannual variations of sea ice mass balance from the central Arctic to the Greenland Sea. *Journal of Geophysical Research: Oceans*, 123(4), 2422–2439. <https://doi.org/10.1002/2017JC013548>
- Leppäranta, M. (2005). *The drift of sea ice*. Springer.
- Leppäranta, M., & Omsted, A. (1990). Dynamic coupling of sea ice and water for an ice field with free boundaries. *Tellus*, 42(4), 4820495–495. <https://doi.org/10.3402/tellusa.v42i4.11892>
- Lombardo, C. P., & Gregg, M. C. (1989). Similarity scaling of viscous and thermal dissipation in a convecting surface boundary layer. *Journal of Geophysical Research*, 94(C5), 6273–6284. <https://doi.org/10.1029/jc094ic05p06273>
- Lozovatsky, I., Figueroa, M., & Roget, E. (2005). Observations and scaling of the upper mixed layer in the North Atlantic. *Journal of Geophysical Research*, 110(C5), C05013. <https://doi.org/10.1029/2004JC002708>
- Martini, K. I., Simmons, H. L., Stoudt, C. A., & Hutchings, J. K. (2014). Near-inertial internal waves and sea ice in the Beaufort Sea. *Journal of Physical Oceanography*, 44(8), 2212–2234. <https://doi.org/10.1175/JPO-D-13-0160.1>
- McPhee, M. G. (1994). On the turbulent mixing length in the oceanic boundary layer. *Journal of Physical Oceanography*, 24(9), 2014–2031. [https://doi.org/10.1175/1520-0485\(1994\)024<2014:ottmli>2.0.co;2](https://doi.org/10.1175/1520-0485(1994)024<2014:ottmli>2.0.co;2)
- McPhee, M. G. (2002). Turbulent stress at the ice/ocean interface and bottom surface hydraulic roughness during the SHEBA drift. *Journal of Geophysical Research*, 107(C10), 8037. <https://doi.org/10.1029/2000JC006633>
- McPhee, M. G. (2008a). *Air-ice-ocean interaction: Turbulent ocean boundary layer exchange process*. Springer.
- McPhee, M. G. (2008b). Physics of early summer ice/ocean exchange in the Western Weddell Sea during ISPOL. *Deep-Sea Research II*, 55(8–9), 1075–1097. <https://doi.org/10.1016/j.dsr2.2007.12.022>
- McPhee, M. G., & Martinson, D. G. (1994). Turbulent mixing under drifting pack ice in the Weddell Sea. *Science*, 263(5144), 218–221. <https://doi.org/10.1126/science.263.5144.218>
- McPhee, M. G., & Stanton, T. P. (1996). Turbulence in the statically unstably oceanic boundary layer under Arctic leads. *Journal of Geophysical Research*, 101(C3), 6409–6428. <https://doi.org/10.1029/95jc03842>
- Morison, J. H., Steele, M., & Anderson, R. (1998). Hydrography of the upper Arctic Ocean measured from the nuclear submarine U.S.S. Pargo. *Deep-Sea Research I*, 45(1), 15–38. [https://doi.org/10.1016/s0967-0637\(97\)00025-3](https://doi.org/10.1016/s0967-0637(97)00025-3)
- Nasmyth, P. W. (1970). *Oceanic turbulence*. Ph.D. thesis. University of British Columbia. <https://doi.org/10.14288/1.0302459>
- Nicolaus, M. (2022). Overview of the MOSAiC expedition — Snow and sea ice. *Elementa Science of the Anthropocene*, 10(1). <https://doi.org/10.1525/elementa.2021.00046>
- Nixdorf, U., Dethloff, K., Rex, M., Shupe, M., Sommerfeld, A., Perovich, D., et al. (2021). *MOSAiC extended acknowledgement*. Zenodo. <https://doi.org/10.5281/zenodo.5179738>
- Oakey, N. S. (1982). Determination of the rate of dissipation of turbulent energy from simultaneous temperature and velocity shear microstructure measurements. *Journal of Physical Oceanography*, 12(3), 256–271. [https://doi.org/10.1175/1520-0485\(1982\)012<0256:dotrod>2.0.co;2](https://doi.org/10.1175/1520-0485(1982)012<0256:dotrod>2.0.co;2)
- Oakey, N. S., & Elliot, J. A. (1982). Dissipation within the surface mixed layer. *Journal of Physical Oceanography*, 12(2), 171–185. [https://doi.org/10.1175/1520-0485\(1982\)012<0171:dwtmsl>2.0.co;2](https://doi.org/10.1175/1520-0485(1982)012<0171:dwtmsl>2.0.co;2)
- Obukhov, A. M. (1971). Turbulence in an atmosphere with a non-uniform temperature. *Boundary-Layer Meteorology*, 2(1), 7–29. <https://doi.org/10.1007/bf00718085>
- Osborn, T. R. (1980). Estimates of the local rate of vertical diffusion from dissipation measurements. *Journal of Physical Oceanography*, 10(1), 83–89. [https://doi.org/10.1175/1520-0485\(1980\)010<0083:eotlro>2.0.co;2](https://doi.org/10.1175/1520-0485(1980)010<0083:eotlro>2.0.co;2)
- Pedlosky, J. (1987). *Geophysical fluid dynamics*. Springer.

- Pinkel, R. (2005). Near-inertial wave propagation in the Western Arctic. *Journal of Physical Oceanography*, 35(5), 645–665. <https://doi.org/10.1175/JPO2715.1>
- Pollard, R. T., & Millard, R. C. (1970). Comparison between observed and simulated wind-generated inertial oscillations. *Deep-Sea Research*, 17(4), 813–816. [https://doi.org/10.1016/0011-7471\(70\)90043-4](https://doi.org/10.1016/0011-7471(70)90043-4)
- Rabe, B., Heuze, C., Regnery, J., Aksenov, Y., Allerholt, J., Athanase, M., et al. (2022). Overview of the MOSAiC expedition: Physical oceanography. *Elementa Science of Anthropocene*, 10(1). <https://doi.org/10.1525/elementa.2021.00062>
- Rampal, P., Weiss, J., Dubois, C., & Campin, J.-M. (2011). IPCC climate models do not capture Arctic sea ice drift acceleration: Consequences in terms of projected sea ice thinning and decline. *Journal of Geophysical Research*, 116, C00D07. <https://doi.org/10.1029/2011JC007110>
- Rampal, P., Weiss, J., & Marsan, D. (2009). Positive trend in the mean speed and deformation rate of Arctic sea ice, 1979–2007. *Journal of Geophysical Research*, 114(C5), C05013. <https://doi.org/10.1029/2008JC005066>
- Richman, J., & Garrett, C. (1977). The transfer of energy and momentum by the wind to the surface mixed layer. *Journal of Physical Oceanography*, 7(6), 876–881. [https://doi.org/10.1175/1520-0485\(1977\)007<0876:ttoeam>2.0.co;2](https://doi.org/10.1175/1520-0485(1977)007<0876:ttoeam>2.0.co;2)
- Rinke, A., Cassano, J. C., Elizabeth, N., Jaiser, R., & Handorf, D. (2020). Meteorological conditions during the MOSAiC expedition: Normal or anomalous? *Elementa Science of Anthropocene*, 9(1). <https://doi.org/10.1525/elementa.2021.00023>
- Rudels, B., Anderson, L. G., & Jones, E. P. (1996). Formation and evolution of the subsurface mixed layer and the halocline of the Arctic Ocean. *Journal of Geophysical Research*, 101(C4), 8807–8821. <https://doi.org/10.1029/96jc00143>
- Schulz, K., Mohrholtz, V., Fer, I., Janout, M., Hoppman, M., Schaffer, J., & Koenig, Z. (2022). A full year of turbulence measurements from a drift campaign in the Arctic Ocean 2019–2020. *Scientific Data*, 9, 472. <https://doi.org/10.1038/s41597-022-01574-1>
- Shaw, W. J., Stanton, T. P., McPhee, M. G., Morison, J. H., & Martinson, D. G. (2009). Role of the upper ocean in the energy budget of Arctic sea ice during SHEBA. *Journal of Geophysical Research*, 114(C6), C06012. <https://doi.org/10.1029/2008JC004991>
- Shirasawa, K. (1986). Water stress and ocean current measurements under first-year sea ice in the Canadian Arctic. *Journal of Geophysical Research*, 91(C12), 14305–14316. <https://doi.org/10.1029/jc091ic12p14305>
- Shirasawa, K., & Ingram, R. G. (1997). Current and turbulent fluxes under the first-year sea ice in Resolute Passage, Northwest Territories, Canada. *Journal of Marine Systems*, 11(1–2), 21–32. [https://doi.org/10.1016/s0924-7963\(96\)00024-3](https://doi.org/10.1016/s0924-7963(96)00024-3)
- Shupe, M. D. (2020). The MOSAiC expedition: A year drifting with the Arctic sea ice. *Arctic Report Card*. <https://doi.org/10.25923/9g3v-xh92>
- Shupe, M. D., Rex, M., Blomquist, B., Persson, P. O. G., Schmale, J., Uttal, T., et al. (2022). Overview of the MOSAiC expedition — Atmosphere. *Elementa Science of the Anthropocene*, 10(1). <https://doi.org/10.1525/elementa.2021.00060>
- Sirevaag, A. (2009). Turbulent exchange coefficients for ice/ocean interface in case of rapid melting. *Geophysical Research Letters*, 36(4), L04606. <https://doi.org/10.1029/2008GL036587>
- Skyllingstad, E. D., Clayton, A. P., Pegau, W. S., McPhee, M. G., & Stanton, T. (2003). Effects of keels on ice bottom turbulence exchange. *Journal of Geophysical Research*, 108(C12), 3372. <https://doi.org/10.1029/2002JC001488>
- Smyth, W. D., & Winters, K. B. (2003). Turbulence and mixing in Holmboe waves. *Journal of Physical Oceanography*, 33(4), 694–711. [https://doi.org/10.1175/1520-0485\(2003\)33<694:tamihw>2.0.co;2](https://doi.org/10.1175/1520-0485(2003)33<694:tamihw>2.0.co;2)
- Strang, E. J., & Fernando, H. J. S. (2001). Entrainment and mixing in stratified shear flows. *Journal of Fluid Mechanics*, 428, 349–386. <https://doi.org/10.1017/s0022112000002706>
- Thorpe, S. A. (1968). A method of producing a shear flow in a stratified fluid. *Journal of Fluid Mechanics*, 32(4), 693–704. <https://doi.org/10.1017/s0022112068000972>
- Thorpe, S. A. (2005). *The turbulent ocean*. Cambridge University Press.
- Timmermans, M.-L., Proshutinsky, A., Krishfield, R. A., Perovich, D. K., Richter-Menge, J. A., Stanton, T. P., & Toole, J. M. (2011). Surface freshening in the Arctic Ocean's Eurasian basin: An apparent consequence of recent change in the wind-driven circulation. *Journal of Geophysical Research*, 116, C00D03. <https://doi.org/10.1029/2011JC006975>
- Toole, J. M., Timmermans, M.-L., Perovich, D. K., Krishfield, R. A., Proshutinsky, A., & Richter-Menge, J. A. (2010). Influence of the ocean surface mixed layer and thermocline stratification on the Arctic sea ice in the central Canada Basin. *Journal of Geophysical Research*, 115(C10), C10018. <https://doi.org/10.1029/2009JC005660>
- Untersteiner, N. (1961). On the mass and heat budget of arctic sea ice. *Arch. Met. Geophys. Bioklim.*, A(12), 151–182. <https://doi.org/10.1007/bf02247491>
- Vivier, F., Hutchings, J. K., Kawaguchi, Y., Kikuchi, T., Morison, J. H., Lourenço, A., & Noguchi, T. (2016). Sea ice melt onset associated with lead opening during the spring/summer transition near the North Pole. *Journal of Geophysical Research: Oceans*, 121(4), 2499–2522. <https://doi.org/10.1002/2015JC011588>
- Wolk, F., Yamazaki, H., Seuront, L., & Lueck, R. G. (2002). A new free-fall profiler for measuring biophysical microstructure. *Journal of Atmospheric and Oceanic Technology*, 19(5), 783–793. [https://doi.org/10.1175/1520-0426\(2002\)019<0780:ANFFPF>2.0.CO;2](https://doi.org/10.1175/1520-0426(2002)019<0780:ANFFPF>2.0.CO;2)
- Zubov, N. N. (1945). *Arctic ice*. Izdatel'stvo Glavmerputi.